A non-overlapping optimized Schwarz method for the heat equation with non linear boundary conditions and with applications to de-icing

Lokman Bennani, Pierre Trontin, Rémi Chauvin, Philippe Villedieu

▶ **To cite this version:**

Lokman Bennani, Pierre Trontin, Rémi Chauvin, Philippe Villedieu. A non-overlapping optimized Schwarz method for the heat equation with non linear boundary conditions and with applications to de-icing. Computers & Mathematics with Applications, 2020, 80 (6), pp.1500-1522. 10.1016/j.camwa.2020.07.017 . hal-02969163

HAL Id: hal-02969163
https://hal.science/hal-02969163v1

Submitted on 16 Oct 2020

HAL is a multi-disciplinary open access archive for the deposit and dissemination of scientific research documents, whether they are published or not. The documents may come from teaching and research institutions in France or abroad, or from public or private research centers.

L'archive ouverte pluridisciplinaire **HAL**, est destinée au dépôt et à la diffusion de documents scientifiques de niveau recherche, publiés ou non, émanant des établissements d'enseignement et de recherche français ou étrangers, des laboratoires publics ou privés.

A non-overlapping optimized Schwarz method for the heat equation with non linear boundary conditions and with applications to de-icing

L. Bennani[a,*], P. Trontin[a], R. Chauvin[b], P. Villedieu[a]

[a] *ONERA / DMPE, Université de Toulouse, F-31055 Toulouse - France*
[b] *CEA / DAM / DIF, F-91680 Bruyères-le-Châtel - France*

Abstract

When simulating complex physical phenomena such as aircraft icing or de-icing, several dedicated solvers often need to be strongly coupled. In this work, a non-overlapping Schwarz method is constructed with the unsteady simulation of de-icing as the targetted application. To do so, optimized coupling coefficients are first derived for the one dimensional unsteady heat equation with linear boundary conditions and for the steady heat equation with non-linear boundary conditions. The choice of these coefficients is shown to guarantee the convergence of the method. Using a linearization of the boundary conditions, the method is then extended to the case of a general unsteady heat conduction problem. The method is tested on simple cases and the convergence properties are assessed theoretically and numerically. Finally the method is applied to the simulation of an aircraft electrothermal de-icing problem in two dimensions.

Keywords: Numerical simulation, Schwarz method, Coupling, Aircraft icing, Electrothermal de-icing

Introduction

The simulation of complex multiphysical phenomena often requires the coupling of several dedicated solvers. As an example, the phenomenon of icing on aircrafts involves many physical aspects such as aerodynamics, droplet trajectories and heat and mass transfer [23]. A typical simulation thus requires the use of several solvers which pass information to each other. The unsteady simulation of thermal de-icing systems requires the coupling between an unsteady thermal model of the de-icing system and an unsteady thermal model of the ice accretion and melting process. As the physical properties of ice and the airfoil are different, the union of these domains is heterogenous. The heat equation is a central element of these models. It is therefore of great interest to conduct an analysis of coupling methods between two domains where the heat equation is to be solved in unsteady (parabolic) or steady (elliptic) form. Also, icing being a complex phenomenon involving for example evaporation or sublimation, the ability to deal with generic boundary conditions is also required. The general context of this work is therefore the coupled solution of the steady or unsteady heat equation on bounded non-overlapping domains with general non-linear boundary conditions.

The coupling of models and codes is an active area of research. Domain decomposition methods form a large family of coupling techniques[24, 22, 10]. Schwarz pioneered this area of research when, in 1870, he showed the existence of the solution of the heat equation on a domain consisting of the overlapping of a rectangle and a disk [21]. The idea is to first solve the heat equation in the disk. Then the resulting solution is used to impose a Dirichlet boundary condition on the rectangle. In turn, the heat equation on the rectangle is solved and provides Dirichlet boundary conditions for the disk. The process is repeated thus generating a sequence of solutions to the heat equation in each domain. Schwarz proved that the sequence

*Corresponding author
Email addresses: lokman.bennani@onera.fr (L. Bennani), pierre.trontin@onera.fr (P. Trontin), remi.chauvin@cea.fr (R. Chauvin), philippe.villedieu@onera.fr (P. Villedieu)

converges which shows the existence of a solution of the heat equation on the union of the disk and the rectangle. This idea has since then be improved and revisited over time [13].

The Schwarz method has been applied to many problems, with and without overlapping [16, 17, 9, 1]. The issue of obtaining optimal coefficients has also been addressed in many different contexts [15, 12, 5]. The general approach is to study the problem on an unbounded domain and use Fourier analysis to derive the conditions and coefficients that guarantee optimal convergence.

For elliptic problems on bounded non-overlapping domains, Lions proposed to use Robin transmission conditions instead of Dirichlet transmission conditions and proved general convergence results[18]. On the outer boundaries Lions considered homogeneous Dirichlet boundary conditions. He noted that the effective choice of the coupling coefficient is not trivial and provided some example for simple geometries. Errera *et al.* derived schemes for the numerical solution of two coupled heat conduction problems[11]. In particular, they studied non-overlapping Robin-Robin transmission conditions and analysed the stability and convergence properties of their approach. Later, Gander *et al.* studied an optimized Schwarz method for the diffusion problem on non-overlapping heterogeneous media[14]. After deriving optimal coefficients using Fourier analysis, they performed numerical tests to demonstrate the efficiency of the method. More recently, Meng *et al.* developed the Conjugate Heat transfer Advanced Multi-domain Partitioned scheme[20]. To do so they use elements of optimal overlapping Schwarz methods with Robin transmission conditions combined with interface jump conditions. The method is demonstrated to be stable for a large range of heat transfer problems. Concerning the external boundary, the previous studies all used linear Dirichlet, Neumann or mixed boundary conditions.

In typical of icing simulations, the evaporative term induces non-linear boundary conditions. Moreover, when simulating the formation or melting of ice, the shape of the different layers, and hence the mesh, changes with time. Moreover, in an industrial context, it is highly desirable that the code simulating the ice protection system and the one simulating the ice accretion and melting be separate. Therefore the goal of this work is to construct a non-overlapping Robin-Robin Schwarz method suited for icing simulation, building upon previous research and the authors' previous work [8].

The article is organized as follows. The idea is to first study and derive coupling coefficients for a one dimensional unsteady heat conduction problem with linear boundary conditions. The next step is to consider a steady state problem with non-linear boundary conditions. The convergence of the method is proved in both of these cases. The two previous steps are then used to propose an extension for the unsteady case with non-linear boundary conditions. Numerical tests are performed to assess the performance of the method. Finally an application to the simulation of electro-thermal de-icing is performed to illustrate the method in more complex situations.

The general setting for the derivation of the method is given by problem (1). It consists of an unsteady coupled heat conduction problem in two domains of different physical properties (see Figure 1) and generic boundary conditions.

$$
\begin{cases}
\rho_1(x)c_1(x)\dfrac{\partial T_1}{\partial t}(t,x) = \dfrac{\partial}{\partial x}\left(\lambda_1(x)\dfrac{\partial T_1}{\partial x}(t,x)\right) & \forall (t,x) \in \mathbb{R}^+ \times \Omega_1 \quad (1a)\\
\rho_2(x)c_2(x)\dfrac{\partial T_2}{\partial t}(t,x) = \dfrac{\partial}{\partial x}\left(\lambda_2(x)\dfrac{\partial T_2}{\partial x}(t,x)\right) & \forall (t,x) \in \mathbb{R}^+ \times \Omega_2 \quad (1b)\\
\lambda_1(-l_1)\dfrac{\partial T_1}{\partial x}(t,-l_1) = f_1\left(T_1\left(t,-l_1\right)\right) & \forall t \in \mathbb{R}^+ \quad (1c)\\
\lambda_2(l_2)\dfrac{\partial T_2}{\partial x}(t,l_2) = -f_2\left(T_2\left(t,l_2\right)\right) & \forall t \in \mathbb{R}^+ \quad (1d)\\
T_1(t,0) = T_2(t,0) & \forall t \in \mathbb{R}^+ \quad (1e)\\
\lambda_1(0)\dfrac{\partial T_1}{\partial x}(t,0) = \lambda_2(0)\dfrac{\partial T_2}{\partial x}(t,0) & \forall t \in \mathbb{R}^+ \quad (1f)
\end{cases}
$$

where t, x and T stand respectively for time, position and temperature. For each domain $i = 1, 2$ ρ_i is the density, c_i the specific heat, λ_i the thermal conductivity, and f_1 and f_2 are increasing and regular enough functions.

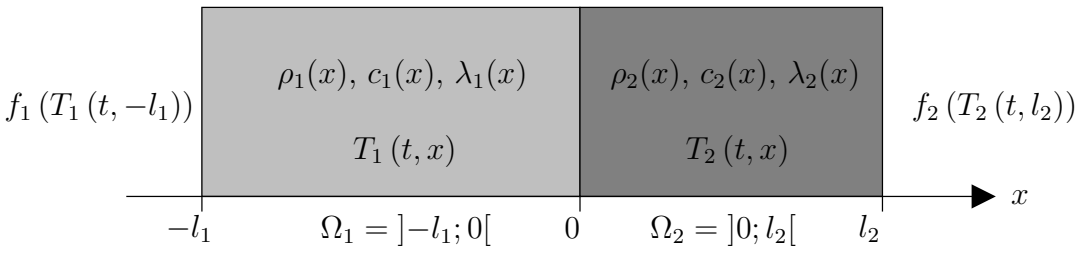

Figure 1: Illustration of the two domains Ω_1 and Ω_2

The goal is to solve each heat conduction problem in its respective domain Ω_i. The domains are coupled through the relations (1e) (continuity of temperature) and (1f) (continuity of heat flux). In the following, this problem is studied by considering two specific problems for which an optimized coupling procedure is derived:

- Unsteady heat conduction with linear boundary conditions.
- Steady heat conduction with general boundary conditions.

These analyses are then used to provide a coupling procedure for the general problem of unsteady heat conduction with general boundary conditions.

1. Unsteady case with linear boundary conditions

In this case, the problem (1) is considered with constant physical properties over each domain and with linear external boundary conditions. More precisely, the functions f_i are assumed to be linear functions of T_i. In order to proceed the time derivative is discretized using an implicit Euler scheme. Discretization is performed using a time step Δt. At the n-th step (where $n \in (N)$) the time is given by $t^n = n\Delta t$. The set of equations hence becomes:

Semi-discrete heat equation in each domain:

$$\rho_1 c_1 \frac{T_1^{n+1} - T_1^n}{\Delta t} = \lambda_1 \frac{d^2 T_1^{n+1}}{dx^2} \qquad \forall x \in \Omega_1 \tag{2a}$$

$$\rho_2 c_2 \frac{T_2^{n+1} - T_2^n}{\Delta t} = \lambda_2 \frac{d^2 T_2^{n+1}}{dx^2} \qquad \forall x \in \Omega_2 \tag{2b}$$

where T_j^n is the temperature field at time step n. Note that the unknown of each equation is T_j^{n+1}.

External boundary conditions:

$$-\lambda_1 \frac{dT_1^{n+1}}{dx}(-l_1) = h_1 \left(T_{r,1} - T_1^{n+1}(-l_1)\right) \tag{2c}$$

$$\lambda_2 \frac{dT_2^{n+1}}{dx}(l_2) = h_2 \left(T_{r,2} - T_2^{n+1}(l_2)\right) \tag{2d}$$

where the constants h_i are heat transfer coefficients and the $T_{r,i}$ represent cooling/heating temperatures.

Interfacial conditions:

$$T_1^{n+1}(0) = T_2^{n+1}(0) \tag{2e}$$

$$\lambda_1 \frac{dT_1^{n+1}}{dx}(0) = \lambda_2 \frac{dT_2^{n+1}}{dx}(0) \tag{2f}$$

where $n_{e,j}$ is the unit normal vector of the external boundary.

By linearity it suffices to consider only the associated homogeneous problems in each domain. To avoid cumbersome notations, T_j^{n+1} is now written simply T_j. The homogeneous problems are defined by:

Semi-discrete homogeneous heat equation in each domain:

$$-\frac{d^2T_1}{dx^2} + \mu_1^2 T_1 = 0 \qquad \forall x \in \Omega_1 \tag{3a}$$

$$-\frac{d^2T_2}{dx^2} + \mu_2^2 T_2 = 0 \qquad \forall x \in \Omega_2 \tag{3b}$$

External boundary conditions:

$$-\lambda_1 \frac{dT_1}{dx}(-l_1) = -h_1 T_1(-l_1) \tag{3c}$$

$$\lambda_2 \frac{dT_2}{dx}(l_2) = -h_2 T_2(l_2) \tag{3d}$$

Interfacial conditions:

$$T_1(0) = T_2(0) \tag{3e}$$

$$\lambda_1 \frac{dT_1}{dx}(0) = \lambda_2 \frac{dT_2}{dx}(0) \tag{3f}$$

where $\mu_j^2 = \frac{\rho_j c_j}{\Delta t \lambda_j}$ $(j = 1, 2)$.

This coupled problem can be solved using a Schwarz algorithm. It defines the sequences $(T_1^{(k)})_{k\in\mathbb{N}}$ and $(T_2^{(k)})_{k\in\mathbb{N}}$ as solutions (in respectively $H^1(\Omega_1)$ and $H^1(\Omega_2)$) to the following problems (see for example [18]):

$$\begin{cases} -\dfrac{d^2T_1^{(k+1)}}{dx^2} + \mu_1^2 T_1^{(k+1)} = 0 \qquad \forall x \in \Omega_1 & \text{(4a)} \\ -\lambda_1 \dfrac{dT_1^{(k+1)}}{dx}(-l_1) = -h_1 T_1^{(k+1)}(-l_1) & \text{(4b)} \\ \lambda_1 \dfrac{dT_1^{(k+1)}}{dx}(0) = \lambda_2 \dfrac{dT_2^{(k)}}{dx}(0) + \omega_1 \left(T_2^{(k)}(0) - T_1^{(k+1)}(0) \right) & \text{(4c)} \end{cases}$$

$$\begin{cases} -\dfrac{d^2T_2^{(k+1)}}{dx^2} + \mu_2^2 T_2^{(k+1)} = 0 \qquad \forall x \in \Omega_2 & \text{(5a)} \\ \lambda_2 \dfrac{dT_2^{(k+1)}}{dx}(l_2) = -h_2 T_1^{(k+1)}(l_2) & \text{(5b)} \\ -\lambda_2 \dfrac{dT_2^{(k+1)}}{dx}(0) = -\lambda_1 \dfrac{dT_1^{(k)}}{dx}(0) + \omega_2 \left(T_1^{(k+1)}(0) - T_2^{(k+1)}(0) \right) & \text{(5c)} \end{cases}$$

where ω_1 and ω_2 are two strictly positive real numbers (the coupling coefficients). The algorithm is initialized with an arbitrary guess of the temperature fields given by T_1^0 and T_2^0. In practice, the temperature field at time t^n can be used as an initializing guess of the solution. One now has to determine whether this algorithm converges or not.

However, by applying the Lax-Milgram theorem [6], it can be shown that in $H^1(]-l_1, l_2[)$ problem (3) has a unique solution given by:

$$T_1(x) = 0 \qquad \forall x \in \Omega_1 \tag{6a}$$

$$T_2(x) = 0 \qquad \forall x \in \Omega_2 \tag{6b}$$

Given the solution (6), the goal is now to determine for which conditions the sequences $(T_1^{(k)})_{k\in\mathbb{N}}$ and $(T_2^{(k)})_{k\in\mathbb{N}}$ converge to 0. Before doing so, let us first introduce some notations. For $i \in 1, 2$, let

$$\chi_i = \exp(-2\mu_i l_i)\frac{\frac{\lambda_i\mu_i}{h_i} - 1}{\frac{\lambda_i\mu_i}{h_i} + 1} \tag{7}$$

$$\xi_i = \frac{\lambda_i\mu_i(1-\chi_i)}{1+\chi_i} \tag{8}$$

Note that as $\lambda_i, \mu_i, h_i, l_i > 0$:

$$-1 < \chi_i < 1 \qquad i = 1, 2 \tag{9}$$

$$\xi_i > 0 \qquad i = 1, 2 \tag{10}$$

The following proposition now provides a criterion to chose the coupling coefficients ω_1 and ω_2.

Proposition 1. *If:*

$$\left|\frac{(\omega_1 - \xi_2)(\omega_2 - \xi_1)}{(\omega_1 + \xi_1)(\omega_2 + \xi_2)}\right| < 1 \tag{11}$$

and $T_1^{(0)}$ and $T_2^{(0)}$ are arbitrary initial guesses for the temperature field then:

$$\begin{cases} \lim_{k\to\infty} T_1^{(k)} = 0 \\ \lim_{k\to\infty} T_2^{(k)} = 0 \end{cases} \tag{12}$$

Proof. The solutions $T_1^{(k)}$ and $T_2^{(k)}$, for $k \geq 1$, to the constant coefficient homogeneous ODEs (4a) and (5a) are:

$$T_1^{(k)} = A_1^{(k)} e^{\mu_1 x} + B_1^{(k)} e^{-\mu_1 x} \tag{13}$$

$$T_2^{(k)} = A_2^{(k)} e^{\mu_2 x} + B_2^{(k)} e^{-\mu_2 x} \tag{14}$$

Inserting (13) into boundary condition (4b) yields:

$$B_1^{(k)} = \chi_1 A_1^{(k)} \tag{15}$$

Moreover, inserting (14) into boundary condition (5b) yields:

$$A_2^{(k)} = \chi_2 B_2^{(k)} \tag{16}$$

First, if $k = 1$ then the coupling boundary conditions (4c) and (5c) give the relations:

$$\begin{aligned} \lambda_1\mu_1\left[A_1^{(1)} - B_1^{(1)}\right] = \lambda_2 \frac{dT_2^{(0)}}{dx}(0) \\ + \omega_1 T_2^{(0)} - \omega_1\left[A_1^{(1)} + B_1^{(1)}\right] \end{aligned} \tag{17}$$

$$\begin{aligned} -\lambda_2\mu_2\left[A_2^{(1)} - B_2^{(1)}\right] = -\lambda_1 \frac{dT_1^{(0)}}{dx}(0) \\ + \omega_2\left(\left[A_1^{(1)} + B_1^{(1)}\right] - \left[A_2^{(1)} + B_2^{(1)}\right]\right) \end{aligned} \tag{18}$$

In combination with (15) and (16), relations (17) and (18) completely determine $A_1^{(1)}$, $B_1^{(1)}$, $A_2^{(1)}$ and $B_2^{(1)}$.

On the other hand for $k \geq 1$, combining (13) with the Fourier-Robin coupling boundary condition (4c), one obtains:

$$\lambda_1\mu_1\left[A_1^{(k+1)} - B_1^{(k+1)}\right] = \lambda_2\mu_2\left[A_2^{(k)} - B_2^{(k)}\right] + \omega_1\left(\left[A_2^{(k)} + B_2^{(k)}\right] - \left[A_1^{(k+1)} + B_1^{(k+1)}\right]\right) \tag{19}$$

Using relations (15) and (16) the previous equation yields:

$$A_1^{(k+1)} = \frac{\omega_1 - \xi_2}{\omega_1\frac{1+\chi_1}{1+\chi_2} + \lambda_1\mu_1\frac{1-\chi_1}{1+\chi_2}} B_2^{(k)} \tag{20}$$

Proceeding the same way with solution (14), the Fourier-Robin coupling boundary condition (5c) and relations (15) and (16) one also obtains:

$$B_2^{(k)} = \frac{\omega_2 - \xi_1}{\omega_2\frac{1+\chi_2}{1+\chi_1} + \lambda_2\mu_2\frac{1-\chi_2}{1+\chi_1}} A_1^{(k)} \tag{21}$$

Combining the two previous relations (20) and (21) yields:

$$A_1^{(k+1)} = \frac{(\omega_1 - \xi_2)(\omega_2 - \xi_1)}{(\omega_1 + \xi_1)(\omega_2 + \xi_2)} A_1^{(k)} \tag{22}$$

Hypothesis (11) implies that:

$$\left|\frac{A_1^{(k+1)}}{A_1^{(k)}}\right| = \left|\frac{B_1^{(k+1)}}{B_1^{(k)}}\right| < 1 \tag{23}$$

Therefore the sequences $\left(A_1^{(k)}\right)_{k\in\mathbb{N}}$ and $\left(B_1^{(k)}\right)_{k\in\mathbb{N}}$ tend to zero as k tends to infinity. Hence:

$$\lim_{k\to\infty} T_1^{(k)} = 0 \tag{24}$$

Moreover, given that for all $k \in \mathbb{N}$, $A_2^{(k)}$ and $B_2^{(k)}$ are proportional to $A_1^{(k)}$ and $B_1^{(k)}$, the sequences $\left(A_2^{(k)}\right)_{k\in\mathbb{N}}$ and $\left(B_2^{(k)}\right)_{k\in\mathbb{N}}$ also tend to zero as k tends to infinity. Therefore:

$$\lim_{k\to\infty} T_2^{(k)} = 0 \tag{25}$$

□

An immediate corrolary of the previous proof is that if one choses $\omega_1 = \xi_2$ and/or $\omega_2 = \xi_1$ then the algorithm converges in one iteration. This hence provides optimal coupling coefficients for the linear unsteady case:

$$\omega_1^\dagger = \xi_2 \tag{26a}$$

$$\omega_2^\dagger = \xi_1 \tag{26b}$$

2. The steady non-linear problem

The steady version of Eq. (1) is now studied. Contrary to the previous section, no simplifying assumptions are made about the boundary conditions and about the distribution of the thermal conductivity λ. T_1 and T_2 are supposed to be functions of the single variable x.

In each domain Ω_i ($i \in \{1,2\}$), Eq. (1a) can be rewritten:

$$\frac{\partial}{\partial x}\left(\lambda_i(x)\frac{\partial T_i}{\partial x}(x)\right) = 0 \qquad \forall x \in \Omega_i \tag{27}$$

For the sake of clarity, the non-linear boundary conditions computed at the outer boundary conditions (Eqs. (1c) and (1d) are reminded:

$$\begin{cases} \lambda_1(-l_1)\dfrac{\partial T_1}{\partial x}(-l_1) = f_1(T_1(-l_1)) & \text{(28a)} \\ \lambda_2(l_2)\dfrac{\partial T_2}{\partial x}(l_2) = -f_2(T_2(l_2)) & \text{(28b)} \end{cases}$$

The same applies to the boundary conditions between the domains Ω_1 and Ω_2 (Eqs. (1e) and (1f):

$$\begin{cases} T_1(0) = T_2(0) & \text{(29a)} \\ \lambda_1(0)\dfrac{\partial T_1}{\partial x}(0) = \lambda_2(0)\dfrac{\partial T_2}{\partial x}(0) & \text{(29b)} \end{cases}$$

To begin with, a usefull result for the remainder of the paper is established:

Proposition 2.

$$\begin{cases} f_1(T_1(-l_1)) = \lambda_1(-l_1)\dfrac{\partial T_1}{\partial x}(-l_1) = \lambda_1(0)\dfrac{\partial T_1}{\partial x}(0) & \text{(30a)} \\ -f_2(T_2(l_2)) = \lambda_2(l_2)\dfrac{\partial T_2}{\partial x}(l_2) = \lambda_2(0)\dfrac{\partial T_2}{\partial x}(0) & \text{(30b)} \end{cases}$$

Proof. The first equality in Eqs. (30a) and (30b) is derived from Eq. (28). Regarding the second equality, $\lambda_i(x)\frac{\partial T_i}{\partial x}(x)$ is constant $\forall x \in \Omega_i$ (Eq. (27). Therefore, $\lambda_1(-l_1)\frac{\partial T_1}{\partial x}(-l_1) = \lambda_1(0)\frac{\partial T_1}{\partial x}(0)$ and $\lambda_2(l_2)\frac{\partial T_2}{\partial x}(l_2) = \lambda_2(0)\frac{\partial T_2}{\partial x}(0)$ which justifies the second equality. □

Using Eq. (29b), a direct consequence of Eqs. (30) from Prop. (2) is:

$$f_1(T_1(-l_1)) = -f_2(T_2(l_2)) \tag{31}$$

The following proposition is a key step in the demonstration process:

Proposition 3. *The two following systems of equations i) and ii) are equivalent:*

i) Initial system composed of Eqs. (27) + (28) + (29)

ii) Eqs. (27) + (28) *with the following additional condition (Eq.* (32)*:*
$T_1(-l_1)$ *and* $T_2(l_2)$ *are the solutions of the system made of the following non linear equations:*

$$\begin{cases} T_1(-l_1) + (l_1r_1 + l_2r_2)\,f_1(T_1(-l_1)) = T_2(l_2) & \text{(32a)} \\ T_2(l_2) + (l_1r_1 + l_2r_2)\,f_2(T_2(l_2)) = T_1(-l_1) & \text{(32b)} \end{cases}$$

where the thermal resistances r_i ($i \in \{1,2\}$) for the domain Ω_i are defined by:

$$r_i \triangleq \frac{1}{l_i}\int_{\Omega_i}\frac{dx}{\lambda_i(x)} \tag{33}$$

Proof. The solution of the problem (27) and (28) is obviously given by:

$$\begin{cases} T_1(x) = T_1(-l_1) + f_1(T_1(-l_1)) \displaystyle\int_{\widehat{\Omega_1}(x)} \frac{dx'}{\lambda_1(x')} & \forall x \in \widehat{\Omega_1} \quad (34a) \\ T_2(x) = T_2(l_2) + f_2(T_2(l_2)) \displaystyle\int_{\widehat{\Omega_2}(x)} \frac{dx'}{\lambda_2(x')} & \forall x \in \widehat{\Omega_2} \quad (34b) \end{cases}$$

where $\widehat{\Omega_1}(x) =]-l_1; x[$ and $\widehat{\Omega_2}(x) =]x; l_2[$. Note that $\widehat{\Omega_1}(0) = \Omega_1$ and $\widehat{\Omega_2}(0) = \Omega_2$. Therefore, from Eq. (34), the only unknowns to be computed to determine the fields T_1 and T_2 in the whole computational domain Ω_1 and Ω_2 respectively are $T_1(-l_1)$ and $T_2(l_2)$. If Eq. (34) is written for $x = 0$, it provides:

$$\begin{cases} T_1(0) = T_1(-l_1) + l_1 r_1 f_1(T_1(-l_1)) & (35a) \\ T_2(0) = T_2(l_2) + l_2 r_2 f_2(T_2(l_2)) & (35b) \end{cases}$$

i)=>ii) Since $T_1(0) = T_2(0)$ (Eq. (29a) and $-f_1(T_1(-l_1)) = f_2(T_2(l_2))$ (Eq. (31), Eq. (32) is derived from Eq. (35).

ii)=>i) Using Eq. (31), Eq. (35) may be rewritten:

$$T_1(0) - T_2(0) = T_1(-l_1) - T_2(l_2) + (l_1 r_1 + l_2 r_2) f_1(T_1(-l_1)) \quad (36)$$

Therefore, from Eq. (32), it provides $T_1(0) = T_2(0)$. A direct consequence of Eqs. (30) and (31) is $\lambda_1(0)\frac{\partial T_1}{\partial x}(0) = \lambda_2(0)\frac{\partial T_2}{\partial x}(0)$. □

The following Schwarz algorithm is proposed between the domains Ω_1 and Ω_2 to find a solution of the system made of Eqs. (27), (28) and (29). Let $T_1^{(k)}$ and $T_2^{(k)}$ two sequences of functions defined iteratively by Eq. (37) and (38).

$$\begin{cases} \dfrac{\partial}{\partial x}\left(\lambda_1(x)\dfrac{\partial T_1^{(k+1)}}{\partial x}(x)\right) = 0 & \forall x \in \Omega_1 \quad (37a) \\ \lambda_1(-l_1)\dfrac{\partial T_1^{(k+1)}}{\partial x}(-l_1) = f_1\left(T_1^{(k+1)}(-l_1)\right) & (37b) \\ \lambda_1(0)\dfrac{\partial T_1^{(k+1)}}{\partial x}(0) = \lambda_2(0)\dfrac{\partial T_2^{(k)}}{\partial x}(0) + \omega_1\left(T_2^{(k)}(0) - T_1^{(k+1)}(0)\right) & (37c) \end{cases}$$

$$\begin{cases} \dfrac{\partial}{\partial x}\left(\lambda_2(x)\dfrac{\partial T_2^{(k+1)}}{\partial x}(x)\right) = 0 & \forall x \in \Omega_2 \quad (38a) \\ \lambda_2(l_2)\dfrac{\partial T_2^{(k+1)}}{\partial x}(l_2) = -f_2\left(T_2^{(k+1)}(l_2)\right) & (38b) \\ \lambda_2(0)\dfrac{\partial T_2^{(k+1)}}{\partial x}(0) = \lambda_1(0)\dfrac{\partial T_1^{(k+1)}}{\partial x}(0) - \omega_2\left(T_1^{(k+1)}(0) - T_2^{(k+1)}(0)\right) & (38c) \end{cases}$$

with ω_1 and ω_2 in $\mathbb{R}^+$.

Proposition 4. *Given the following hypothesis:*

$$\begin{cases} \omega_1 = 1/(r_2 l_2) & (39a) \\ \omega_2 = 1/(r_1 l_1) & (39b) \\ \exists \kappa_1 \in \mathbb{R}^{+\star}, \quad \forall x \in \mathbb{R}, \quad f_1'(x) \geq \kappa_1 & (39c) \\ \exists \kappa_2 \in \mathbb{R}^{+\star}, \quad \forall x \in \mathbb{R}, \quad f_2'(x) \geq \kappa_2 & (39d) \end{cases}$$

the sequences $T_1^{(k)}$ *and* $T_2^{(k)}$ *are convergent for every initial solution. More precisely: for every initial solution* $T_1^{(0)}$ *and* $T_2^{(0)}$ *which satisfy Eqs.* (27) *and* (28)*, we have* $T_1^{(k)} \underset{k\to\infty}{\longrightarrow} T_1$ *and* $T_2^{(k)} \underset{k\to\infty}{\longrightarrow} T_2$ *where* T_1 *and* T_2 *are the solutions of Eqs.* (27)*,* (28) *and* (29)*.*

Proof. From Prop. (2) the previous algorithm can be rewritten:

$$\begin{cases} \dfrac{\partial}{\partial x}\left(\lambda_1(x)\dfrac{\partial T_1^{(k+1)}}{\partial x}(x)\right) = 0 \qquad \forall x \in \Omega_1 & \text{(40a)} \\ \lambda_1(-l_1)\dfrac{\partial T_1^{(k+1)}}{\partial x}(-l_1) = f_1\left(T_1^{(k+1)}(-l_1)\right) & \text{(40b)} \\ f_1\left(T_1^{(k+1)}(-l_1)\right) = -f_2\left(T_2^{(k)}(l_2)\right) + \omega_1\left(T_2^{(k)}(0) - T_1^{(k+1)}(0)\right) & \text{(40c)} \end{cases}$$

$$\begin{cases} \dfrac{\partial}{\partial x}\left(\lambda_2(x)\dfrac{\partial T_2^{(k+1)}}{\partial x}(x)\right) = 0 \qquad \forall x \in \Omega_2 & \text{(41a)} \\ \lambda_2(l_2)\dfrac{\partial T_2^{(k+1)}}{\partial x}(l_2) = -f_2\left(T_2^{(k+1)}(l_2)\right) & \text{(41b)} \\ -f_2\left(T_2^{(k+1)}(l_2)\right) = f_1\left(T_1^{(k+1)}(-l_1)\right) - \omega_2\left(T_1^{(k+1)}(0) - T_2^{(k+1)}(0)\right) & \text{(41c)} \end{cases}$$

We focus now on the sequences $T_1^{(k)}(-l_1)$ and $T_2^{(k)}(l_2)$. Using Eq. (35), the equations (40c) and (41c) may be written:

$$\begin{cases} f_1\left(T_1^{(k+1)}(-l_1)\right) &=& -f_2\left(T_2^{(k)}(l_2)\right) \\ &+& \omega_1\left(T_2^{(k)}(l_2) + l_2 r_2 f_2\left(T_2^{(k)}(l_2)\right) - T_1^{(k+1)}(-l_1) - l_1 r_1 f_1\left(T_1^{(k+1)}(-l_1)\right)\right) \\ -f_2\left(T_2^{(k+1)}(l_2)\right) &=& f_1\left(T_1^{(k+1)}(-l_1)\right) \\ &-& \omega_2\left(T_1^{(k+1)}(-l_1) + l_1 r_1 f_1\left(T_1^{(k+1)}(-l_1)\right) - T_2^{(k+1)}(l_2) - l_2 r_2 f_2\left(T_2^{(k+1)}(l_2)\right)\right) \end{cases} \tag{42}$$

which may be rewritten using hypothesis (39a) and (39b):

$$\begin{cases} G_1\left(T_1^{(k+1)}(-l_1)\right) = T_2^{(k)}(l_2) + (l_2 r_2 - 1/\omega_1) f_2\left(T_2^{(k)}(l_2)\right) & \text{(43a)} \\ G_2\left(T_2^{(k+1)}(l_2)\right) = T_1^{(k+1)}(-l_1) + (l_1 r_1 - 1/\omega_2) f_1\left(T_1^{(k+1)}(-l_1)\right) & \text{(43b)} \end{cases}$$

where G_1 and G_2 are defined as:

$$\begin{cases} G_1(x) \triangleq x + \left(l_1 r_1 + \dfrac{1}{\omega_1}\right) f_1(x) & \text{(44a)} \\ G_2(x) \triangleq x + \left(l_2 r_2 + \dfrac{1}{\omega_2}\right) f_2(x) & \text{(44b)} \end{cases}$$

From hypothesis (39c) and (39d), it can be written:

$$\begin{cases} G_1'(x) > 1 + \left(l_1 r_1 + \dfrac{1}{\omega_1}\right)\kappa_1 \qquad \forall x \in \mathbb{R} & \text{(45a)} \\ G_2'(x) > 1 + \left(l_2 r_2 + \dfrac{1}{\omega_2}\right)\kappa_2 \qquad \forall x \in \mathbb{R} & \text{(45b)} \end{cases}$$

which means that G_1 and G_2 are invertible functions. Equation (45) allows to limit the derivatives of the inverse functions $g_1 = G_1^{-1}$ and $g_2 = G_2^{-1}$:

$$\begin{cases} 0 < g_1'(x) \leq \dfrac{1}{1 + (l_1 r_1 + 1/\omega_1)\,\kappa_1} < 1 & \forall x \in \mathbb{R} \quad (46a) \\ 0 < g_2'(x) \leq \dfrac{1}{1 + (l_2 r_2 + 1/\omega_2)\,\kappa_2} < 1 & \forall x \in \mathbb{R} \quad (46b) \end{cases}$$

Equation (43) may be rewritten:

$$\begin{cases} T_1^{(k+1)}(-l_1) = g_1 \circ p_1\left(T_2^{(k)}(l_2)\right) & (47a) \\ T_2^{(k+1)}(l_2) = g_2 \circ p_2\left(T_1^{(k+1)}(-l_1)\right) & (47b) \end{cases}$$

where the functions p_1 and p_2 are given by:

$$\begin{cases} p_1(x) \triangleq x + (l_2 r_2 - 1/\omega_1)\, f_2(x) & \forall x \quad (48a) \\ p_2(x) \triangleq x + (l_1 r_1 - 1/\omega_2)\, f_1(x) & \forall x \quad (48b) \end{cases}$$

Therefore Eq. (47) can be written:

$$T_2^{(k+1)}(l_2) = g_2 \circ p_2 \circ g_1 \circ p_1\left(T_2^{(k)}(l_2)\right) \quad (49)$$

From hypothesis (39a) and (39b),the functions p_1 and p_2 are the function identity and $T_2^{(k+1)}(l_2) = g_2 \circ g_1\left(T_2^{(k)}(l_2)\right)$. Let $A \in \mathbb{R}^{+*}$ and $(x, y) \in [-A; A]$. According to the mean value equality on $[-A; A]$:

$$|g_2 \circ g_1(x) - g_2 \circ g_1(y)| \leq \sup_{z \in [-A;A]} |(g_2 \circ g_1)'(z)| \cdot |x - y| \quad (50)$$

where $\sup_{z \in [-A;A]} |(g_2 \circ g_1)'(z)| < \sup_{z \in \mathbb{R}^+} |(g_2 \circ g_1)'(z)| < 1$ from Eq. (46). Therefore, the function $g_2 \circ g_1$ is a contractant function, has a single fixed point $T_1(-l_1)$ and $T_1^{(k)}(-l_1) \underset{k \to +\infty}{\longrightarrow} T_1(-l_1)$. By analogous reasoning, it can be shown that $g_1 \circ g_2$ is a contractant function, has a single fixed point $T_2(l_2)$ and $T_2^{(k)}(l_2) \underset{k \to +\infty}{\longrightarrow} T_2(l_2)$. After a passage to the limit in Eq. (43), $T_1(-l_1)$ and $T_2(l_2)$ are the solution of Eqs. (32). Therefore, from Prop. (3), the limit functions T_1 and T_2 of the sequences $T_1^{(k)}$ and $T_2^{(k)}$ are solutions of the problem (27) + (28) + (29). □

An optimized version of the presented Schwarz algorithm is now presented. To do this, another definition for the coefficients ω_1 and ω_2 is proposed so as to define a "more contractant" function $g_2 \circ p_2 \circ g_1 \circ p_1$ (Eq. (49)). One way to proceed is to cancel the derivative $p_1'\left(T_2^{(k)}(l_2)\right)$:

$$p_1'\left(T_2^{(k)}(l_2)\right) = 0 \Longleftrightarrow \left(\omega_1^{(k+1)}\right)^{\dagger\dagger} = \left(l_2 r_2 + \frac{1}{f_2'(x_2^{(k)})}\right)^{-1} \quad (51)$$

ω_1 changes over iterations k. Similarly, it is shown that:

$$\left(\omega_2^{(k+1)}\right)^{\dagger\dagger} = \left(l_1 r_1 + \frac{1}{f_1'(x_1^{(k+1)})}\right)^{-1} \quad (52)$$

Note that chosing the coefficients $\left(\omega_1^{(k+1)}\right)^{\dagger\dagger}$ and $\left(\omega_2^{(k+1)}\right)^{\dagger\dagger}$ allows to increase the convergence speed. However, the convergence of the Schwarz algorithm is not ensured since the condition (32) is not verified.

3. Unsteady case with general boundary conditions

The two previous sections dealt with:

- the coupling between two unsteady problems with linear boundary conditions and constant physical properties in each domain.
- the coupling between two steady problems with generic boundary conditions and non constant physical properties in each domain.

The goal is now to combine the results of these two previous sections to construct a coupling algorithm for the generic unsteady problem (1). To do so, the coefficients (26a) and (26b) are extended using mean values of physical properties over each domain. As in section (1), the starting is the time discrete heat equation:

Semi-discrete heat equation in each domain:

$$\mathcal{L}_1 T_1^{n+1} = \mu_1^2 T_1^n \qquad \forall x \in \Omega_1 \tag{53a}$$

$$\mathcal{L}_2 T_2^{n+1} = \mu_2^2 T_2^n \qquad \forall x \in \Omega_2 \tag{53b}$$

External boundary conditions:

$$-\lambda_1(-l_1)\frac{dT_1^{n+1}}{dx}(-l_1) = -f_1\left(T_1^{n+1}(-l_1)\right) \tag{53c}$$

$$\lambda_2(l_2)\frac{dT_2^{n+1}}{dx}(l_2) = -f_2\left(T_2^{n+1}(l_2)\right) \tag{53d}$$

Interfacial conditions:

$$T_1^{n+1}(0) = T_2^{n+1}(0) \tag{53e}$$

$$\lambda_1(0)\frac{dT_1^{n+1}}{dx}(0) = \lambda_2(0)\frac{dT_2^{n+1}}{dx}(0) \tag{53f}$$

where $\mu_j(x) = \frac{\rho_j(x)c_j(x)}{\Delta t \lambda_j(x)}$ is now not necessarily uniform and the operator $\mathcal{L}_j$ is defined as:

$$\mathcal{L}_j T = -\frac{1}{\lambda_j}\frac{d}{dx}\left(\lambda_j \frac{dT}{dx}\right) + \mu_j^2 T \tag{54}$$

In addition, the mean values of the parameters are introduced:

$$\widehat{\rho_j c_j} = \frac{1}{l_j}\int_{\Omega_j} \rho_j c_j \, dx \tag{55a}$$

$$r_j = \frac{1}{l_j}\int_{\Omega_j} \frac{dx}{\lambda_j} \tag{55b}$$

$$\widehat{\mu_j} = \sqrt{\frac{\widehat{\rho_j c_j}\widehat{r_j}}{\Delta t}} \tag{55c}$$

The Schwarz coupling algorithm to solve this problem is given by:

$$\begin{cases} \mathcal{L}_1 T_1^{(k+1)} = \mu_1^2 T_1^n \ \forall x \in]-l_1, 0[& (56a) \\ -\lambda_1 \dfrac{dT_1^{(k+1)}}{dx}(-l_1) = -f_1\left[T_1^{(k+1)}(-l_1)\right) & (56b) \\ \lambda_1 \dfrac{dT_1^{(k+1)}}{dx}(0) = \lambda_2 \dfrac{dT_2^{(k)}}{dx}(0) + \omega_1\left(T_2^{(k)}(0) - T_1^{(k+1)}(0)\right) & (56c) \end{cases}$$

$$\begin{cases} \mathcal{L}_2 T_2^{(k+1)} = \mu_2^2 T_2^n \ \forall x \in]0, l_2[& \text{(57a)} \\ \lambda_2 \dfrac{dT_2^{(k+1)}}{dx}(l_2) = -f_2\left(T_1^{(k+1)}(l_2)\right) & \text{(57b)} \\ -\lambda_2 \dfrac{dT_2^{(k+1)}}{dx}(0) = -\lambda_1 \dfrac{dT_1^{(k)}}{dx}(0) + \omega_2\left(T_1^{(k+1)}(0) - T_2^{(k+1)}(0)\right) & \text{(57c)} \end{cases}$$

In order to define the coupling coefficients at iteration $k+1$, the idea is to linearise the boundary conditions (56b) and (57b) around the solution at iteration k. For example, noting $\Delta_{T,k} = T_1^{(k+1)}(-l_1) - T_1^{(k)}(-l_1)$, the right hand side of (56b) may be written:

$$-f_1\left(T_1^{(k+1)}(-l_1)\right) = -\left[f_1\left(T_1^{(k)}(-l_1)\right) + \Delta_{T,k} f_1'\left(T_1^{(k)}(-l_1)\right) + O(\Delta_{T,k}^2)\right] \tag{58}$$

By analogy with section 1 the coefficients $\eta_j^{(k+1)}$, χ_j and $\omega_j^{(k+1)}$ are defined by:

$$\begin{cases} \eta_1^{(k+1)} = \dfrac{\widehat{\mu_1}}{r_1 f_1'\left(T_1^{(k)}(-l_1)\right)} & \text{(59a)} \\ \eta_2^{(k+1)} = \dfrac{\widehat{\mu_2}}{r_2 f_2'\left(T_2^{(k)}(l_2)\right)} & \text{(59b)} \end{cases}$$

$$\chi_j = \exp(-2\widehat{\mu_j} l_j)\frac{\eta_j^{(k+1)} - 1}{\eta_j^{(k+1)} + 1} \tag{60}$$

$$\begin{cases} \omega_1^{(k+1)} = \dfrac{\widehat{\mu_2}}{r_2}\dfrac{1 - \chi_2^{(k+1)}}{1 + \chi_2^{(k+1)}} & \text{(61a)} \\ \omega_2^{(k+1)} = \dfrac{\widehat{\mu_1}}{r_1}\dfrac{1 - \chi_1^{(k+1)}}{1 + \chi_1^{(k+1)}} & \text{(61b)} \end{cases}$$

As stated previously, this definition is made by analogy with the unsteady linear problem and there is no apriori guarantee that the algorithm will converge with this choice of coupling coefficients. However, as will be shown in the following section, the algorithm performs well in generic conditions such as those encountered in icing applications. Moreover, one has the following interesting property:

Proposition 5. *In the limit $\Delta t \to \infty$, the coupling coefficients* (61) *are given by (51) and (52), that is to say the optimized values derived for the steady state case.*

Proof. An asymptotic analysis is required in order to obtain the behaviour of the coupling coefficients when $\Delta t \to \infty$. First note that $\lim_{\Delta t \to \infty} \widehat{\mu_j} = 0$ $(j = 1, 2)$. Also, the coupling coefficients are of the form:

$$\omega = \frac{X}{r}\frac{1 - e^{-2lX}\frac{aX-1}{aX+1}}{1 + e^{-2lX}\frac{aX-1}{aX+1}} \tag{62}$$

with the following generic notations:

- X: $\widehat{\mu_1}$ or $\widehat{\mu_2}$
- l: l_1 or l_2
- r: r_1 or r_2
- a: $\left(r_1 f_1'\left(T_1^{(k)}(-l_1)\right)\right)^{-1}$ or $\left(r_2 f_2'\left(T_2^{(k)}(l_2)\right)\right)^{-1}$

Given the following Taylor expansions:

$$\frac{aX-1}{aX+1} = -1 + 2aX + O(X^2) \tag{63}$$

$$\exp(-2lX) = 1 - 2lX + O(X^2) \tag{64}$$

one obtains:

$$\exp(-2lX)\frac{aX-1}{aX+1} = -1 + 2(a+l)X + O(X^2) \tag{65}$$

Hence:

$$1 - \exp(-2lX)\frac{aX-1}{aX+1} = 2 - 2(a+l)X + O(X^2) \tag{66a}$$

$$1 + \exp(-2lX)\frac{aX-1}{aX+1} = 2(a+l)X + O(X^2) \tag{66b}$$

Therefore:

$$\omega = \frac{X}{r}\frac{1 - e^{-2lX\,\frac{aX-1}{aX+1}}}{1 + e^{-2lX\,\frac{aX-1}{aX+1}}} \tag{67a}$$

$$= \frac{X}{r}\frac{2 - 2(a+l)X + O(X^2)}{2(a+l)X + O(X^2)} \tag{67b}$$

$$= \frac{2X + O(X^2)}{2\left(ra + rl\right)X + O(X^2)} \tag{67c}$$

Therefore, in the limit $\Delta t \to \infty$, hence $X \to 0$, the coupling coefficients reduce to:

$$\omega_1 = \left(l_2 r_2 + \frac{1}{f_2'\left(T_2^{(k)}(l_2)\right)}\right)^{-1} \tag{68a}$$

$$\omega_2 = \left(l_1 r_1 + \frac{1}{f_1'\left(T_1^{(k)}(-l_1)\right)}\right)^{-1} \tag{68b}$$

where the values of a, l and r have been replace by their respective counterparts. Therefore, when $\Delta t \to \infty$, the coupling coefficients reduce to the steady-state values given by (51) and (52).

□

4. Numerical examples

In this section, the algorithm is illustrated by considering two test cases. Each test case consists in solving problem (1), illustrated in Figure 1, with a specific set of material parameters and boundary conditions. The numerical implementation is based on an implicit finite difference scheme using classical Euler time discretization and second order spatial finite difference scheme for the diffusion term.

4.1. Linear case

Consider the problem as illustrated in Figure 2. A block of a given material of length $2l = 0.02m$ is initially at $T(x,0) \triangleq T_i = 300K$. Here the block is homogeneous and split only for the purpose of the test case into two subdomains of length $l_1 = 0.005m$ and $l_2 = 0.015m$.

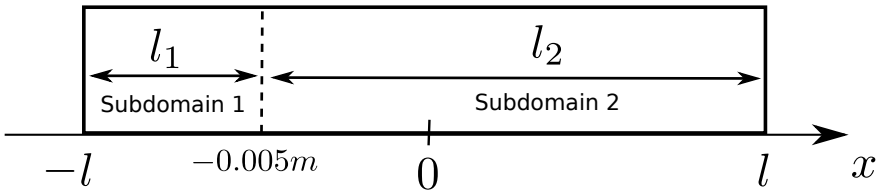

Figure 2: Illustration of the unsteady linear test case

The physical properties are uniform and given in Table 1. The block is subjected to convective heat transfer on both boundaries. The boundary heat transfer characteristics are given in Table 1. In this case the functions f_1 and f_2 are given by:

$$f_1\left(T_1\left(-l\right)\right) = h_{tc}\left(T_1\left(-l\right) - T_r\right) \tag{69a}$$

$$f_2\left(T_2\left(l\right)\right) = h_{tc}\left(T_2\left(l\right) - T_r\right) \tag{69b}$$

$\rho\ (kg.m^{-3})$	$c_p\ (J.kg^{-1}.K^{-1})$	$\lambda\ (W.m^{-1}.K^{-1})$	$h_{tc}\ (W.m^{-2}.K^{-1})$	$T_r\ (K)$
2700	900	100	400	340

Table 1: Material properties and heat transfer characteristics for the first test case

This problem has an analytical solution given by [25, 19]:

$$\frac{T - T_r}{T_i - T_r} = \sum_{n=1}^{\infty} A_n \cos(k_n \frac{x}{l}) e^{-k_n^2 F_o} \tag{70}$$

where

$$F_o = \frac{\alpha t}{l^2} \tag{71a}$$

$$\alpha = \frac{\lambda}{\rho c_p} \tag{71b}$$

and

$$A_n = \frac{\sin(k_n)}{k_n + \sin(k_n)\cos(k_n)} \tag{72}$$

and the k_n's are solutions of the equation:

$$k_n \tan(k_n) = B_i \tag{73}$$

where B_i is the Biot number defined by: $B_i = \frac{h_{tc} l}{\lambda}$.

In order to test the performance of the algorithm, the domain is split at $x = -0.005m$. The solution can then be obtained by solving the heat equation on each sub-domain and using the unsteady coupling procedure previously defined (56 and 57). The computation is run with a time step of $0.1s$ and optimized coupling coefficients (given by equations (61a) and (61b)). At every time step, the coupling procedure is performed until the relative temperature difference and relative difference of heat flux at the interface both have values below 10^{-6}.

As shown in Figure 3, the numerical solution is in excellent agreement with the analytical one (given by equation (70)). The convergence criterion was met within two coupling iterations over the whole simulation.

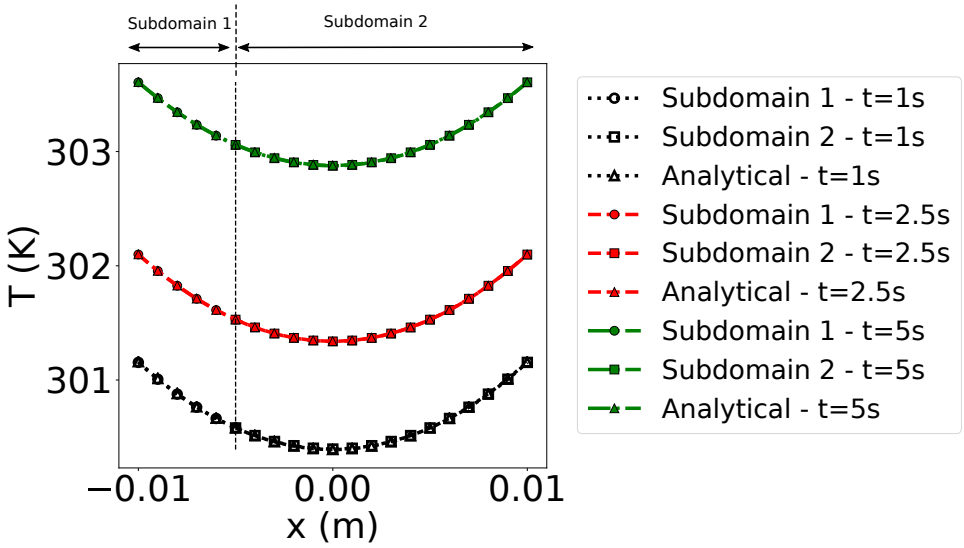

Figure 3: Comparison of numerical and analytical solutions (using optimized coupling coefficients)

In addition, one may also evaluate the numerical convergence properties of the algorithm over one time step. Figure 4 shows the relative differences in temperature and heat flux at the interface, at each iteration of the Schwarz algorithm and at $t = 1s$. In order to perform a comparative study the simulation is also run with non optimal coefficients. The coupling coefficients given by (39a) and (39b) are chosen as the non-optimal ones. When using optimal coefficients, the rate of convergence is much higher. After two iterations the differences is well below the acceptable tolerance for practical applications.This is coherent with the fact that in the semi-discrete case, these optimal coefficients guarantee convergence in one iteration (as discussed at the end of section 1). On the other hand, the use of non-optimal coupling coefficients induces a lagrer amount of iterations to satisfy the convergence criterion.

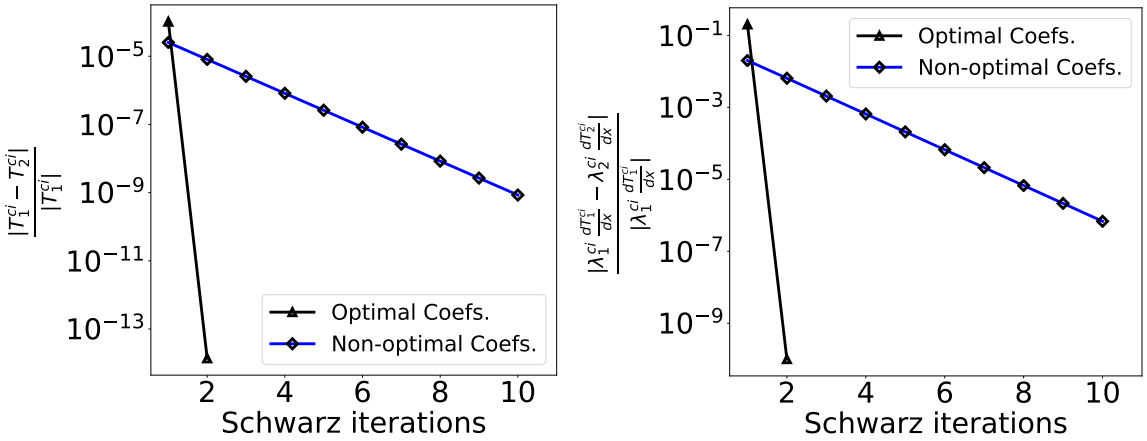

(a) Relative temperature difference at interface

(b) Relative flux difference at interface

Figure 4: Relative differences in temperature and flux and the interface using optimal and non-optimal coupling coefficients (at $t = 1s$). The superscript ci means that the values are taken at the coupling interface.

4.2. Non-linear case

The case considered in this section, illustrated by Figure 1, consists of two different materials in contact each with uniform physical properties given in Table 2. One of them is only subjected to convective heat transfer while the other is also subject to evaporation. In this case, the function f_1 and f_2 are given by:

$$f_1\left(T_1\left(-l_1\right)\right) = \dot{m}_{ev}(T_1\left(-l_1\right))\left(c_{p,1}T_1\left(-l_1\right) + L_v(T_1\left(-l_1\right))\right) + h_{tc,1}\left(T_1\left(-l_1\right) - T_{r,1}\right) \tag{74a}$$

$$f_2\left(T_2\left(l_2\right)\right) = h_{tc,2}\left(T_2\left(l_2\right) - T_{r,2}\right) \tag{74b}$$

where $\dot{m}_{ev}$ is the evaporation rate and L_v is the latent heat of vaporisation (see Appendix A for further details. For this case $T_\infty = 280K$, $p_\infty = 98000Pa$ and $p_e = 98000Pa$). Note that the evaporation rate is a non linear function of temperature.

Material	ρ_i $(kg.m^{-3})$	$c_{p,i}$ $(J.kg^{-1}.K^{-1})$	λ_i $(W.m^{-1}.K^{-1})$	$h_{tc,i}$ $(W.m^{-2}.K^{-1})$	$T_{r,i}$ (K)
1	1000	4181	0.6	200	313.15
2	2700	900	167	500	300

Table 2: Material properties and heat transfer characteristics for the second test case ($i = 1, 2$)

In this case, f_1 is non-linear. Figure 5 shows the numerical solution at $t = 1s$, $t = 5s$ and $t = 10s$. Due to the evaporative cooling, the temperature at the left boundary decreases rapidly. At every time step, the coupling procedure is performed until the relative temperature difference and relative difference of heat flux at the interface both have values below 10^{-6}. The convergence criterion was met within two coupling iterations over the whole simulation.

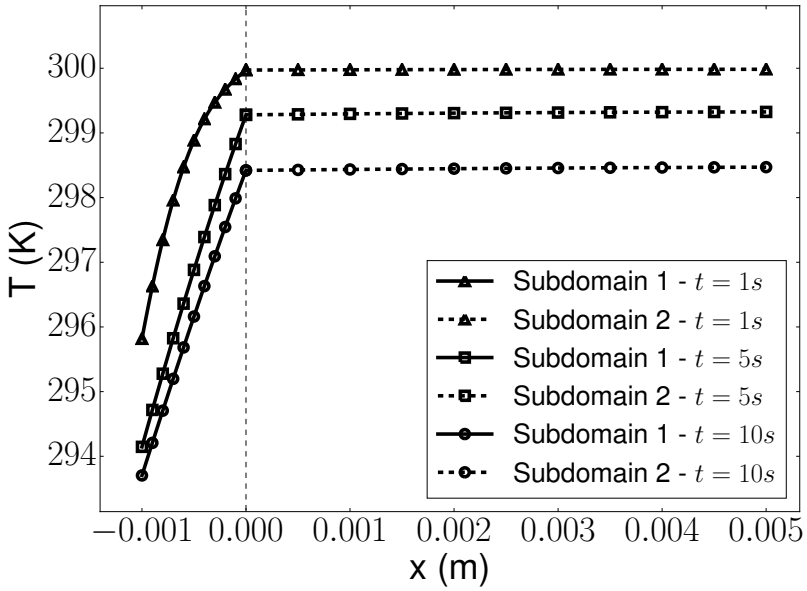

Figure 5: Temperature field at $t = 1s$, $t = 5s$ and $t = 10s$

In order to evaluate the convergence properties in this case, the procedure of the previous section is repeated (for $t = 5s$). The results are shown in Figure 6. As in the previous case, the optimized set of coefficients yields a much higher rate of convergence. Note that in this case, the theoretical background regarding the convergence properties is much weaker than in the linear case. Therefore, this test case also serves as a numerical investigation of the convergence properties of the methodology in a general setting.

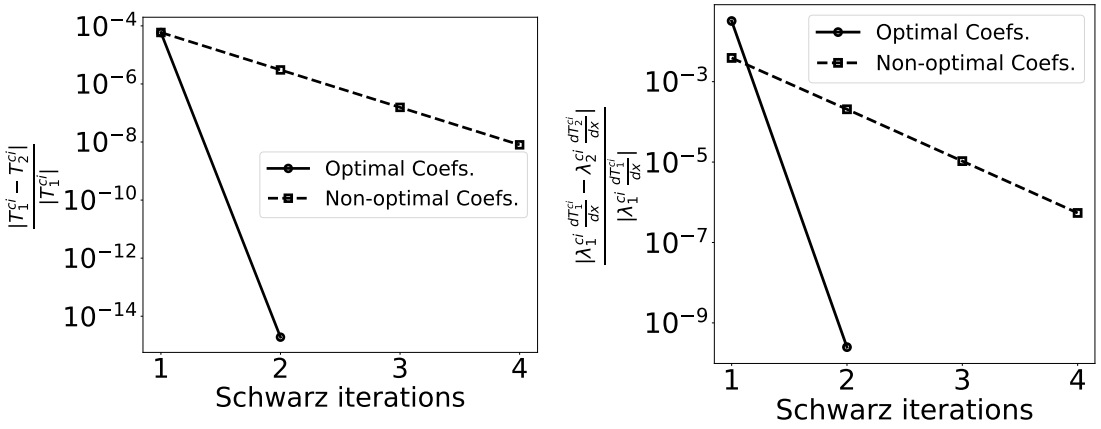

(a) Relative temperature difference at interface

(b) Relative flux difference at interface

Figure 6: Relative differences in temperature and flux and the interface using optimal and non-optimal coupling coefficients (at $t = 5s$). The superscript ci means that the values are taken at the coupling interface.

5. Application to Electrothermal De-Icing

An application to the phenomenon of aircraft icing and ice protection is now considered. Icing is due to the presence in clouds of supercooled water droplets. Upon impacting an aircrafts surface, the metastable supercooled state of the droplets is broken. At that point, the droplets undergo a liquid-solid phase change, leading to ice bluid-up on the impinged surface. This phenomenon has many undesirable consequences and manufacturers must therefore equip their aircraft with ice protection systems.

This case deals with the simulation of electrothermal de-icing. First, let's recall the typical operating of an electro-thermal de-icing system. Consider the case where an airfoil has to be protected from the build up of ice on its surface. To do so, one may place several heater mats within the thickness of the airfoil and activate them according to a given power cycle. During this power cycle ice may build up or melt and liquid water may run downstream under the effect of the aerodynamic forces. This may lead to several possible states as illustrated in Figure 7b [7].

The simulation of the thermal behaviour of an electro-thermal de-icing system therefore requires two solvers. One that solves the heat conduction problem in the skin of the airfoil, composed of several layers of materials and electrical heaters. Another that solves the unsteady phase change problems of ice accretion and melting. In this work, a finite volume solver called ETIPS2D is used to simulate the electro-thermal system (see [2] for a description). Concerning the unsteady ice accretion and melting problem, an unsteady mixed finite volume-Galerkin solver called MiLeS2D is used (see [7] for a detailled description). A global illustration is shown in Figure 7b.

In order to perform the simulation of the electro-thermal de-icer in icing conditions, the two previously mentionned solvers are coupled using the Schwarz method presented in section 3. Here the simulation is two dimensional and both meshes are coincident. The coupling method is extended by performing a locally one dimensional coupling. More precisely, for each interfacial edge only the normal cells to that edge are used to compute the coupling coefficients (see Figure 7a).

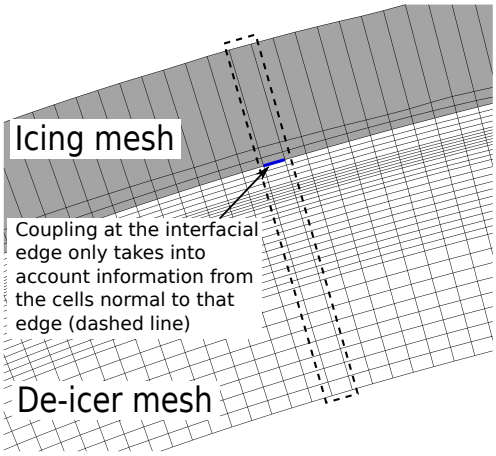

(a) Example of coincident meshes and cells used for coupling procedure

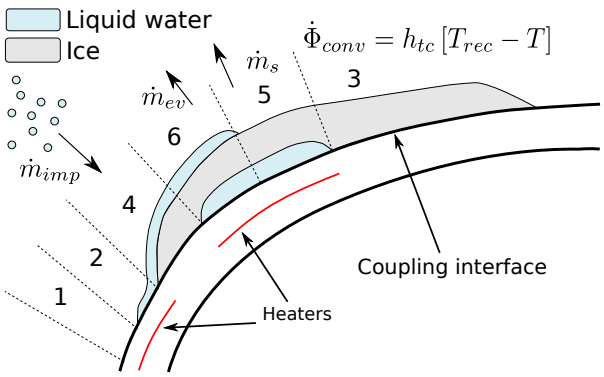

(b) Global illustration of the case. Several states are possible for the icing process leading to different mass and energy transfer terms (see [7] for details)

Figure 7: Differences in temperature and flux and the interface at $t = 39.1s$ showing convergence with a low number of iterations.

Before moving to the test case, note that MiLeS2D has a complex algorithmic structure, the explicit tracking of phase change fronts requiring to take into account several possible states and possible shifts between these states. The six possible states, illustrated in Figure 7b, are defined as:

1. Full evaporative: the whole mass of impacting droplets is evaporated (for example, due to heat provided by an ice protection system).
2. Running wet: only a liquid water film is present. Under the action of the aerodynamic forces, the liquid film runs back along the surface.
3. Rime accretion: the droplets freeze almost instantaneously leading to ice build up with no liquid water.
4. Glaze accretion: the droplets freeze, but at a slower rate than in the rime case. Therefore, a running liquid water film is present on top of the ice layer.
5. Rime accretion with melting at the surface (due to heat provided by an ice protection system for example).
6. Glaze accretion with melting at the surface (due to heat provided by an ice protection system for example).

So as to illustrate the complexity of the algorithm, suppose for example that an ice layer is present (rime ice state). If the heater mat is activated, this will lead to the melting of the ice. This means that at that point in time, the state must be switched from rime ice to rime ice with static film. More precisely, at each time step, the algorithm will first start by assuming the same state as in the previous time step. If this yields a result compatible with the current state, the solution is conserved and the algorithm proceeds. However, if an incompatibility is detected (for example the temperature of the ice is greater than the melting temperature), the algorithm switches to another mode. As will be discussed later, this can lead to jumps in the Schwarz coupling procedure. Indeed, switching from one state to another changes the flux at the interface and hence directly impacts the coupling algorithm. Figure 8 illustrates the general architecture for the simulation.

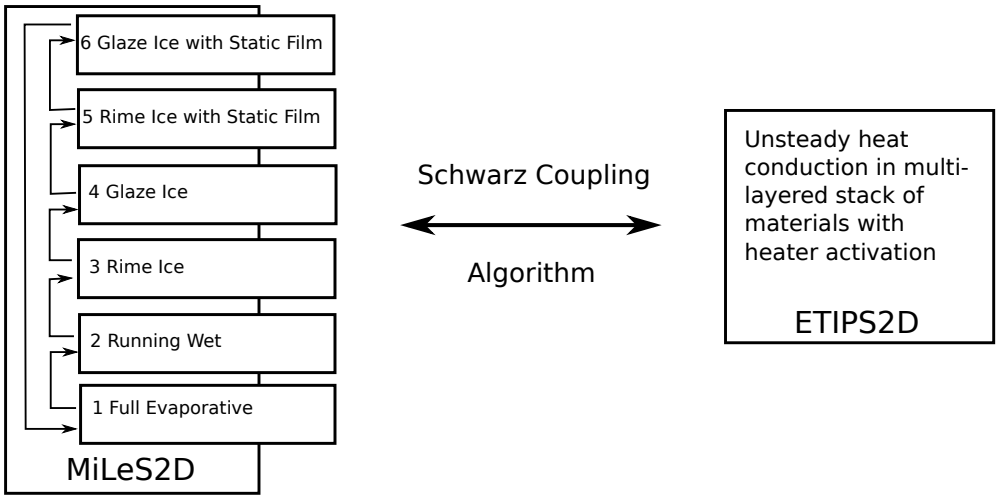

Figure 8: General architecture of the numerical simulation procedure involving MiLeS2D and ETIPS2D.

5.1. Description of the case

This illustrative test case consists of a de-iced NACA0012 airfoil in icing conditions. The droplets start impacting after $5s$ of activation of the system. The aerodynamic and icing conditions are given in Table 3.

Chord (m)	α $(^\circ)$	T_∞ (K)	P_∞ (Pa)	M_∞	MVD (μm)	LWC $(g.m^{-3})$
0.6	0	253.15	79470	0.5	20	0.34

Table 3: Aerodynamic and icing conditions for the de-iced NACA0012 case

The airfoil is made out of a multi-layered material whose properties are provided in Table 4. The layers are numbered from outer to inner as shown in Figure 9.

Layer no	c_p $(J.kg^{-1}.K^{-1})$	ρ $(kg.m^{-3})$	λ $(W.m^{-1}.K^{-1})$	thickness (m)
1	2350	1000	17.03	8.e-04
2	2009	1000	0.293	3.e-04
3	2381	1000	0.313	1.e-04
4	2009	1250	0.293	2.e-04
5	2009	1250	0.293	5.e-04
6	1717	1000	0.25	2.52e-03
7	1717	1000	0.25	4.e-03

Table 4: Layer thicknesses and material properties

Heater mats are embedded into the stack of materials between layers 4 and 5. They are shown in Figure 9 and are labelled PS, HM1 and HM2. The heater mat located at the leading edge is comonly refered to as the parting strip (hence the label PS). The locations of the heater mats (in terms of curvilinear abscissa, where $s = 0$ at the leading edge) are given by:

- PS located between $s_1 = -0.015625\,m$ and $s_2 = 0.015625\,m$.
- HM1 located between $s_1 = -0.048875\,m$ and $s_2 = -0.017625\,m$.
- HM2 located between $s_1 = 0.017625\,m$ and $s_2 = 0.048875\,m$.

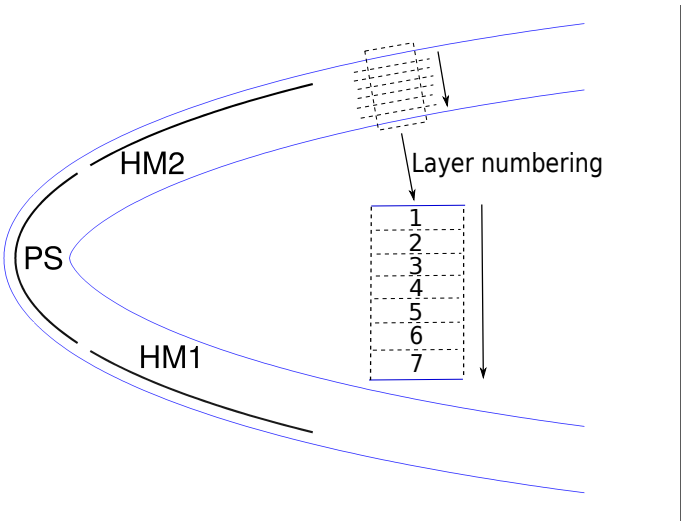

Figure 9: De-icing heater layout

Numerically, the coupling method requires a convergence criterion. To do so, the following quantities are considered:

$$\epsilon_T = \max_{\Gamma_i} \left(|T_{\Gamma_i}^{MiLeS} - T_{\Gamma_i}^{ETIPS}| \right) \tag{75}$$

where $T_{\Gamma_i}^{MiLeS}$ and $T_{\Gamma_i}^{ETIPS}$ are the temperatures at the interfacial edge Γ_i computed by MiLeS2D and ETIPS2D respectively. The maximum is taken over all edges of the coupling interface.

$$\epsilon_\phi = \max_{\Gamma_i} \left(\frac{|\phi_{n_i}^{MiLeS} - \phi_{n_i}^{ETIPS}|}{|\phi_{n_i}^{ETIPS}|} \right) \tag{76}$$

where $\phi_{n_i}^{MiLeS}$ and $\phi_{n_i}^{ETIPS}$ are the heat fluxes normal to the i-th coupling interface Γ_i, computed by MiLeS2D and ETIPS2D respectively. In this case, the coupling loops is considered converged if ϵ_T and ϵ_ϕ fall below 0.001.

This type of simulation is embedded within a larger simulation chain called IGLOO2D [23]. Computations of the inviscid flow around the airfoil, boundary layer flow and droplet trajectories are performed prior to the presented coupled simulation. Relevant data are given in Appendix B.

Two variants of this configuration are simulated. The differences are in the heater mat power cycles. They are therefore refered to as "activation cycle 1" and "activation cycle 2". In both cases, during the first five seconds of simulation the mat PS is activated with no droplet impact. The cases are symmetric with respect to the x-axis and therefore the results are presented only at the upper part of the airfoil.

5.2. Activation cycle 1

This activation power cycle ($t = 0s$ corresponds to the beginning of the cycle and the whole cycle lasts for $80s$) is given by:

- PS activated at $t = 0s$ with a power density of $50kW.m^{-2}$. Activation lasts $80s$.
- HM1 activated at $t = 40s$ with a power density of $25kW.m^{-2}$. Activation lasts $40s$.
- HM2 activated at $t = 40s$ with a power density of $25kW.m^{-2}$. Activation lasts $40s$.

Figure 10 shows the resulting temperature field at $t = 5s$, just before droplets start to impact. The region where the heater mat's power is applied is clearly visible.

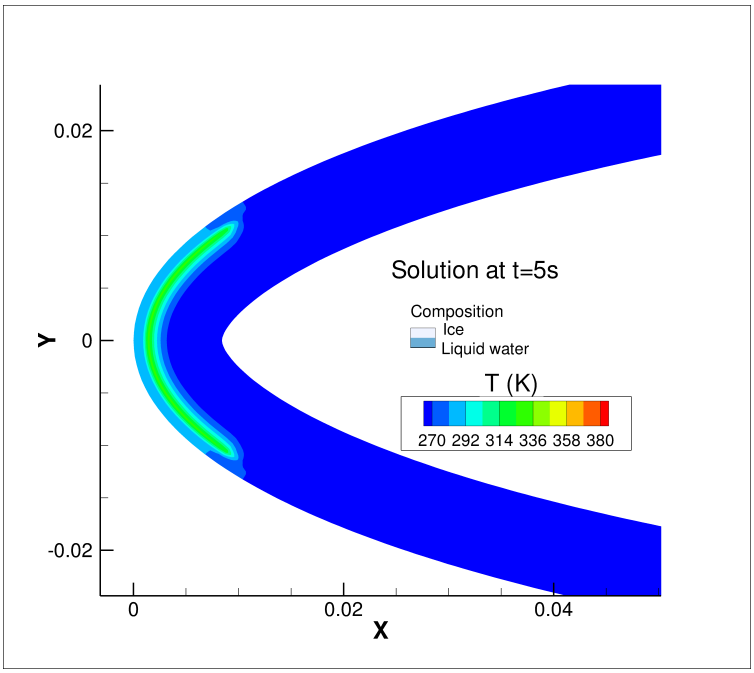

Figure 10: Solution at $t = 5s$

At $t = 5s$, droplets start to impact the airfoil and ice starts to build-up beyond the region heated by PS. This can be observed in Figure 11 which shows the temperature field in the airfoil, the ice shape and the dynamic liquid film (height scaled by a factor 500 for visualisation purposes) at $t = 40s$.

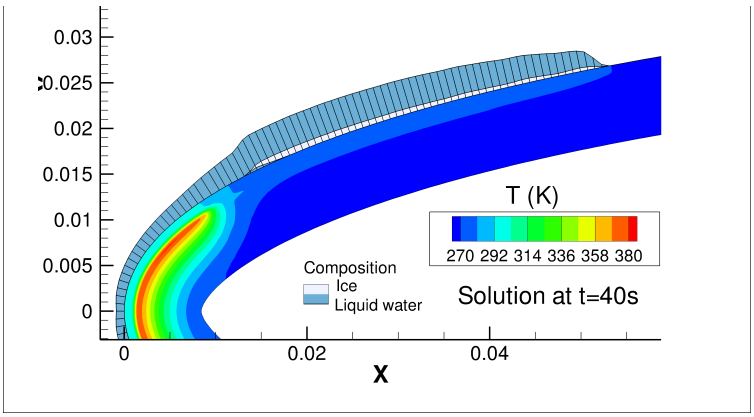

Figure 11: Solution at $t = 40s$ (the running film height is scaled by a factor 500 for visualisation purposes)

At $t = 40s$ the heaters HM1 and HM2 are activated. The heat melts the ice layer above those mats. Therefore, a static film layer is created underneath the ice, as shown in Figure 12.

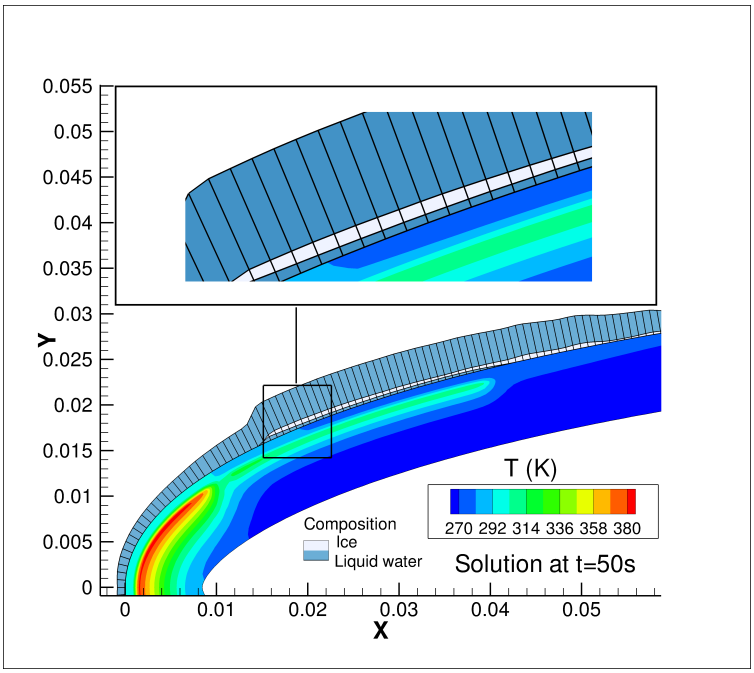

Figure 12: Solution at $t = 50s$ (the running film height is scaled by a factor 500 for visualisation purposes)

The activation of HM1 and HM2 eventually melts all the ice layer in their respective heated regions. At the end of the simulation ($t = 80s$) water has now runback and frozen beyond the protected region (see Figure 13).

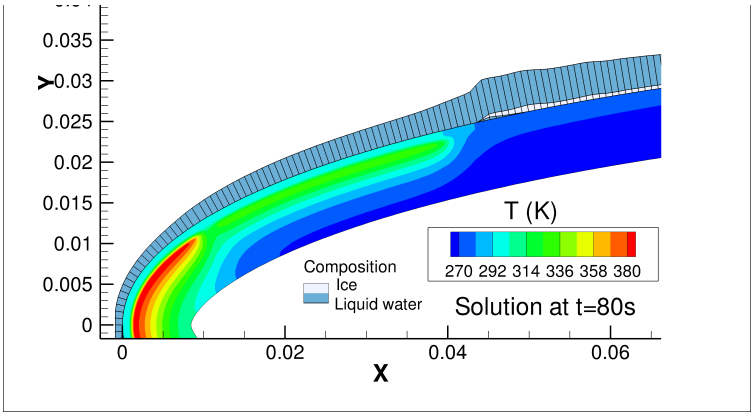

Figure 13: Solution at $t = 80s$ (the running film height is scaled by a factor 500 for visualisation purposes)

As stated earlier, the ice accretion model is complex and non-linear. Moreover, the heater mats are taken into account thanks to a source term which was not accounted for in the theoretical derivation of the Schwarz coupling method. There is no theoretical guarantee of the convergence of the coupling procedure. Nevertheless, the situation is close enough to those of sections 1 and 2 for the method to exhibit globally good convergence properties in practice. To illustrate this point let's consider two extreme convergence cases.

Figure 14 shows the convergence curve for the absolute difference in temperature and relative difference in flux at the interface at $t = 39.1s$. At that time step, the coupling procedure converges rapidly. The values fall below the given tolerance of 0.001 after five iterations.

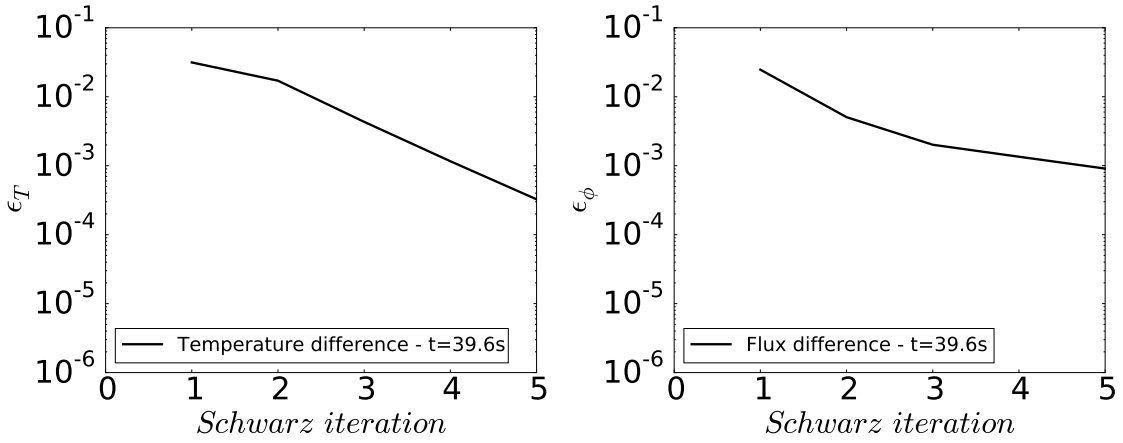

(a) Temperature difference at interface

(b) Flux difference at interface

Figure 14: Differences in temperature and flux and the interface at $t = 39.1s$ showing convergence with a low number of iterations.

On the other hand, certain time steps may require more iterations to converge. As discussed previously (see Fig. 8), depending on the thermal state of the system the ice accretion solver may be required to switch modes in order to obtain the solution at a given time step. As this changes the fluxes at the coupling interface, this can induce convergence issues as shown in Figure 15. Nevertheless, convergence is still reached.

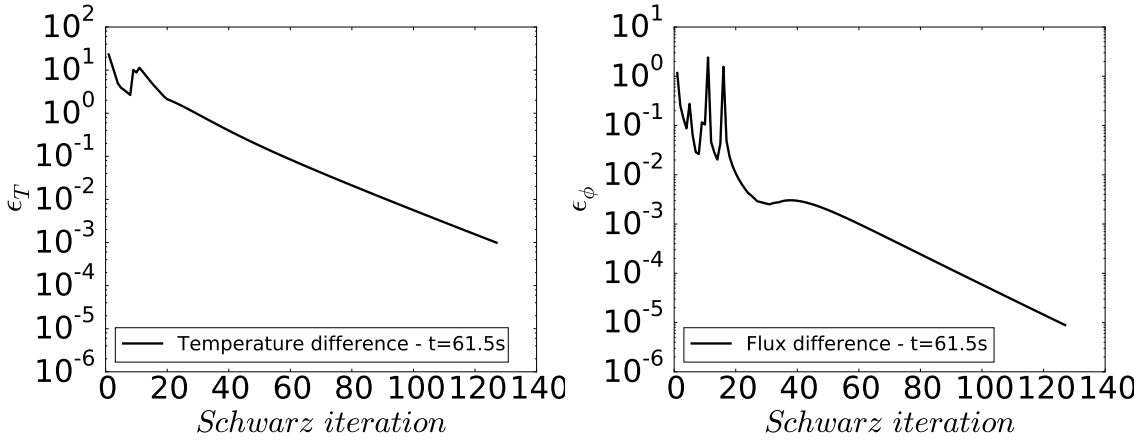

(a) Temperature difference at interface

(b) Flux difference at interface

Figure 15: Differences in temperature and flux and the interface at $t = 61s$ showing difficulty in convergence.

One may ask which behaviour is most frequently observed in practice. Figure 16 is a histogram representing, over the whole simulation, the number of times a given amount of Schwarz iterations was required for convergence. The average number of Schwarz iterations was 17. Moreover, Figure 16 shows that the most frequent behaviour is a number of Schwarz iterations less than 20. Hence, the cases where convergence is highly slowed down by mode switching remain reasonable.

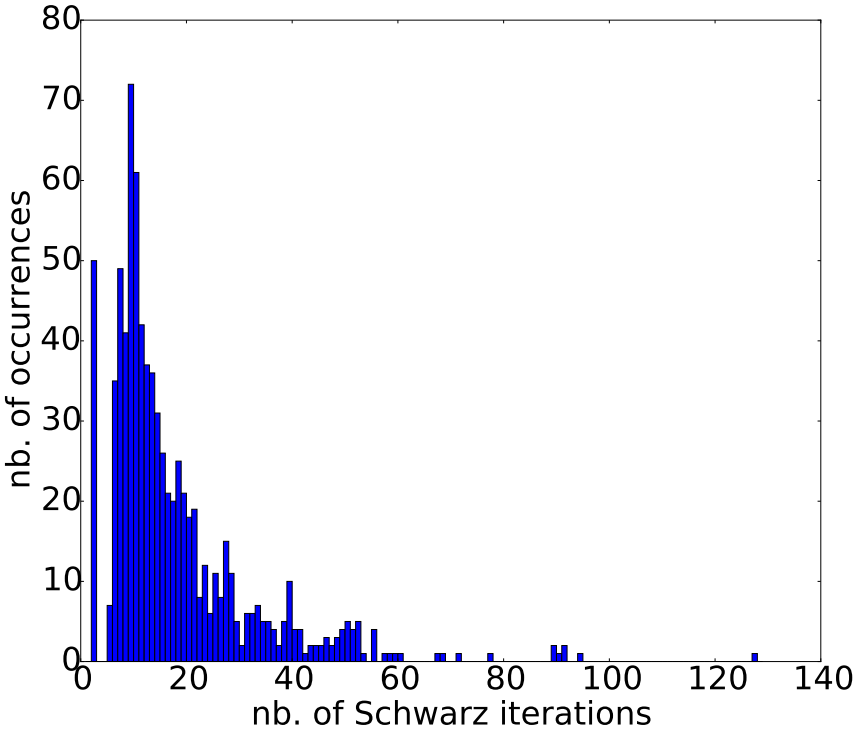

Figure 16: Number of occurences for each possible number of Schwarz iterations (activation cycle 1). The average number of iterations is 17.

To get a more complete view of the convergence of the coupling algorithm during the simulation the number of iterations required at each time step to reach the desired convergence criterion is shown in Figure 17. Even though some spikes with a high number of iterations are visible, 20 to 25 iterations are usually sufficient.

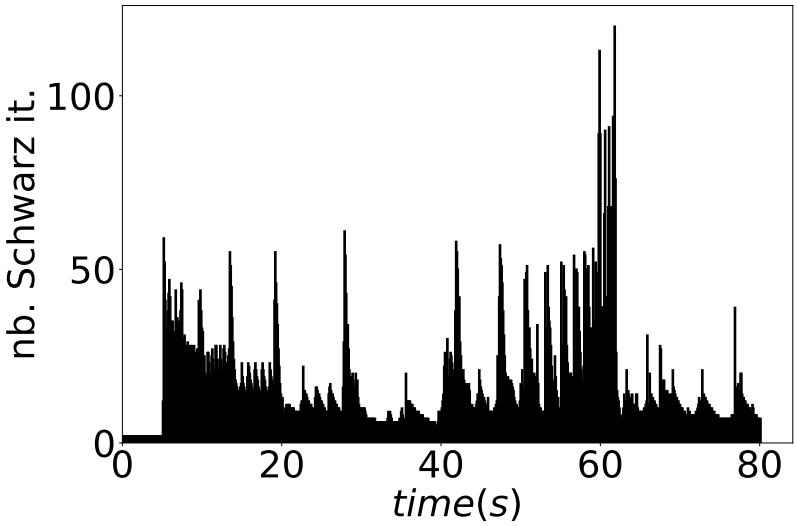

Figure 17: Number of Schwarz iterations at every time step (activation cycle 1).

5.3. Activation cycle 2

In second activation power cycle HM1 and HM2 are deactivated then reactived during the cycle. The cycle is given by:

- PS activated at $t = 0s$ with a power density of $50kW.m^{-2}$. Activation lasts $80s$.
- HM1 activated from $t = 40s$ to $t = 50s$ and reactivated from $t = 60s$ to $t = 70s$ with a power density of $25kW.m^{-2}$.
- HM2 activated from $t = 40s$ to $t = 50s$ and reactivated from $t = 60s$ to $t = 70s$ with a power density of $25kW.m^{-2}$.

Up to $t = 50s$ this case is identical to the previous one. At $t = 50s$ heaters HM1 and HM2 are deactivated. Ice is able to continue to build up while the skin temperature decreases. Figure 18 shows that at $t = 60s$, just before the reactivation of HM1 and HM2, a small layer of ice is still present.

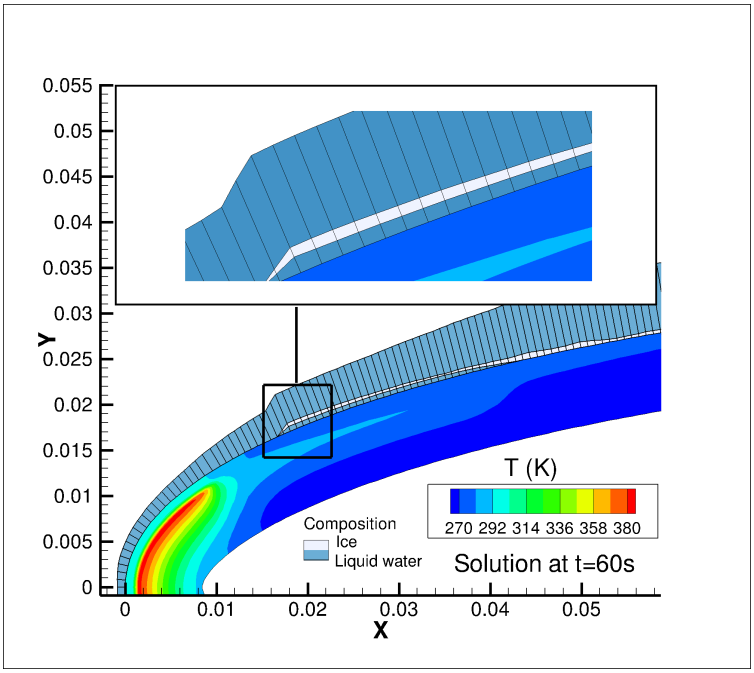

Figure 18: Solution at $t = 60s$ (the running film height is scaled by a factor 500 for visualisation purposes)

This layer of ice is progressively melted by the heat provided by HM1 and HM2 after their reactivation. Figure 19 shows the result at $t = 72s$. Even though HM1 and HM2 are now deactivated again, the thin ice layer continues to melt due to thermal inertia.

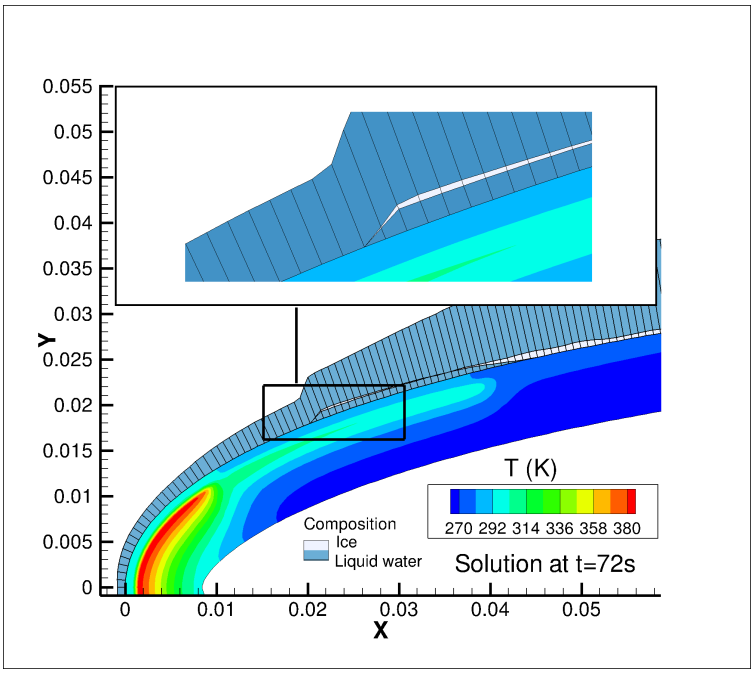

Figure 19: Solution at $t = 60s$ (the running film height is scaled by a factor 500 for visualisation purposes)

At $t = 80s$ the area where the heater mats are located is completely free of ice. However, the running back liquid film generates ice build up beyond the protected area.

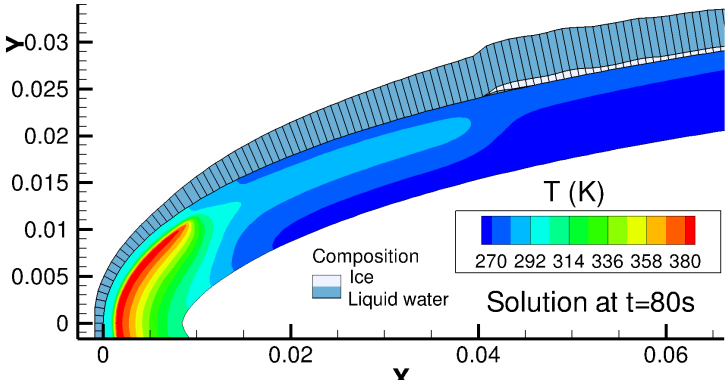

Figure 20: Solution at $t = 80s$ (the running film height is scaled by a factor 500 for visualisation purposes)

As in the previous case, Figure 21 is a histogram representing, over the whole simulation, the number of times a given amount of Schwarz iterations was required for convergence. The behaviour is similar. For some time steps a large number of coupling iterations was required. However the average number of iterations was 18.

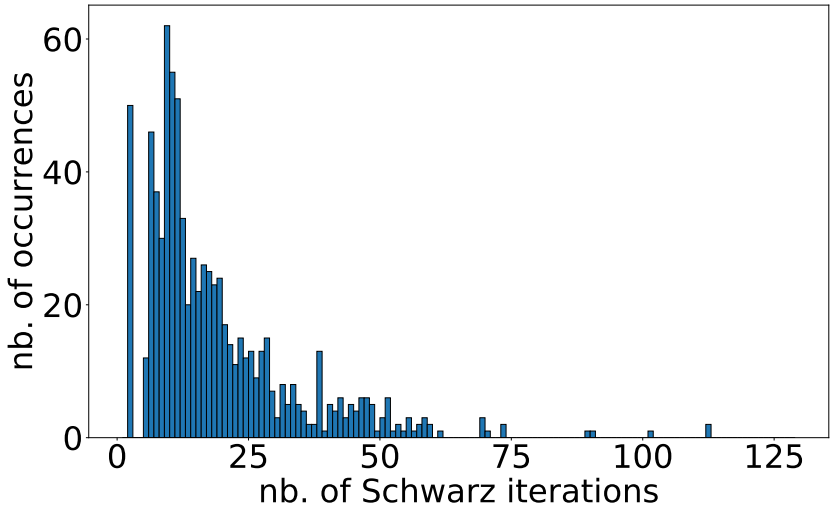

Figure 21: Number of occurences for each possible number of Schwarz iterations (activation cycle 2).

Finally, Figure 22 shows the number of coupling iterations required to reach the convergence criterion at every time step. The spikes reflect the fact that for some time steps the convergence of the coupling procedure is slow. Nevertheless, in most cases, 25 iterations are sufficient.

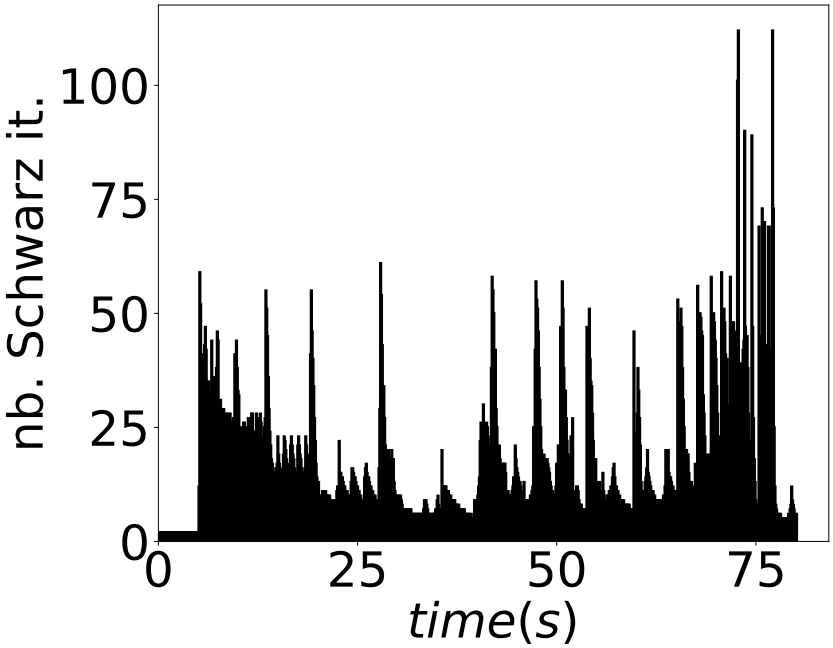

Figure 22: Number of Schwarz iterations at every time step (activation cycle 2).

6. Conclusion

This paper focuses on a Schwarz coupling methodology. The goal was to obtain coupling coefficients which could be used to solve coupled heat transfer problems in generic settings. To do so, two cases where

theoretical derivations are possible were presented: the unsteady case with linear boundary conditions and the steady case with general boundary conditions. The coefficients obtained with these derivations guarantee the convergence of the algorithm. Moreover, the theoretical derivation also provided the framework to obtain optimized coupling coefficients. In order to treat unsteady cases with generic boundary conditions, the coefficients obtained for linear boundary conditions are extended using a linearisation of the boundary conditions.

Two numerical test cases are then performed in order to assess the effective convergence properties of the coupling algorithm. The results for the first test case showed an excellent agreement with the analytical solution. Moreover, for both test cases, the algorithm was shown to efficiently converge. In addition, the numerical investigation also showed that using the optimal set of coefficients yielded a much higher rate of convergence.

Finally, an electro-thermal de-icing case was simulated using this method to couple two unsteady solvers. Although in some occurences convergence was slowed down by the mode switching of the ice accretion solver, the method performed well. Some improvements, such as accounting for the heater mat source terms in the derivation of the coupling coefficients, are possible and are part of ongoing work.

The perspectives of this work is to be able to fully simulate the behaviour of an electrothermal ice protection system. One of the last elements to be added is the modelling, simulation and understanding of the ice shedding phenomenon. This requires a mechanical model of the ice blocks and poses the problem of characterizing the physical properties of atmospheric ice. Some work in this direction has already been performed [4, 3]. The next step is to integrate this model into the present coupling procedure.

7. Acknowledgements

The work presented in this paper was funded by ONERA (Office National d'Etudes et de Recherches Aérospatiales) and DGA (Direction Générale de l'Armement). Their financial support is gratefully acknowledged.

Bibliography

[1] Hubert Alcin, Bruno Koobus, Olivier Allain, and Alain Dervieux. Efficiency and scalability of a two-level schwarz algorithm for incompressible and compressible flows. *International Journal for Numerical Methods in Fluids*, 72(1):69–89, 2013.

[2] Lokman Bennani, Philippe Villedieu, and Michel Salaun. Two dimensional model of an electro-thermal ice protection system. In *5th AIAA Atmospheric and Space Environments Conference*, page 2936, 2013.

[3] Lokman Bennani, Philippe Villedieu, and Michel Salaun. A mixed adhesion–brittle fracture model and its application to the numerical study of ice shedding mechanisms. *Engineering Fracture Mechanics*, 158:59–80, 2016.

[4] Lokman Bennani, Philippe Villedieu, Michel Salaun, and Pierre Trontin. Numerical simulation and modeling of ice shedding: Process initiation. *Computers & Structures*, 142:15–27, 2014.

[5] Daniel Bennequin, Martin J Gander, Loic Gouarin, and Laurence Halpern. Optimized schwarz waveform relaxation for advection reaction diffusion equations in two dimensions. *Numerische Mathematik*, 134(3):513–567, 2016.

[6] Haim Brezis. *Functional analysis, Sobolev spaces and partial differential equations*. Springer Science & Business Media, 2010.

[7] Rémi Chauvin, Lokman Bennani, Pierre Trontin, and Philippe Villedieu. An implicit time marching galerkin method for the simulation of icing phenomena with a triple layer model. *Finite Elements in Analysis and Design*, 150:20–33, 2018.

[8] Rémi Chauvin, Philippe Villedieu, and Pierre Trontin. A robust coupling algorithm applied to thermal ice protection system unsteady modeling. In *6th AIAA Atmospheric and Space Environments Conference*, page 2061, 2014.

[9] Clark R Dohrmann and Olof B Widlund. An overlapping schwarz algorithm for almost incompressible elasticity. *SIAM Journal on Numerical Analysis*, 47(4):2897–2923, 2009.

[10] Victorita Dolean, Pierre Jolivet, and Frédéric Nataf. *An introduction to domain decomposition methods: algorithms, theory, and parallel implementation*, volume 144. SIAM, 2015.

[11] Marc-Paul Errera and Sébastien Chemin. Optimal solutions of numerical interface conditions in fluid–structure thermal analysis. *Journal of Computational Physics*, 245:431–455, 2013.

[12] Martin J Gander. Optimized schwarz methods. *SIAM Journal on Numerical Analysis*, 44(2):699–731, 2006.

[13] Martin J Gander. Schwarz methods over the course of time. *Electron. Trans. Numer. Anal*, 31(5):228–255, 2008.

[14] Martin J Gander and Olivier Dubois. Optimized schwarz methods for a diffusion problem with discontinuous coefficient. *Numerical Algorithms*, 69(1):109–144, 2015.

[15] Martin J Gander, Frédéric Magoules, and Frédéric Nataf. Optimized schwarz methods without overlap for the helmholtz equation. *SIAM Journal on Scientific Computing*, 24(1):38–60, 2002.

[16] Martin J Gander and Hongkai Zhao. Overlapping schwarz waveform relaxation for the heat equation in n dimensions. *BIT Numerical Mathematics*, 42(4):779–795, 2002.
[17] Pierre Gosselet and Christian Rey. Non-overlapping domain decomposition methods in structural mechanics. *Archives of computational methods in engineering*, 13(4):515, 2006.
[18] Pierre-Louis Lions. On the schwarz alternating method. iii: a variant for nonoverlapping subdomains. In *Third international symposium on domain decomposition methods for partial differential equations*, volume 6, pages 202–223. SIAM Philadelphia, PA, 1990.
[19] Alexei V Luikov. *Analytical heat diffusion theory*. Elsevier, 2012.
[20] Fanlong Meng, Jeffrey W Banks, William D Henshaw, and Donald W Schwendeman. A stable and accurate partitioned algorithm for conjugate heat transfer. *Journal of Computational Physics*, 344:51–85, 2017.
[21] Hermann A Schwarz. über einen grenzübergang durch alternierendes verfahren. *Vierteljahrsschrift der Naturforschenden Gesellschaft in Zürich*, 15:272–286, 1870.
[22] Andrea Toselli and Olof Widlund. *Domain decomposition methods-algorithms and theory*, volume 34. Springer Science & Business Media, 2006.
[23] Pierre Trontin, Ghislain Blanchard, Alexandros Kontogiannis, and Philippe Villedieu. Description and assessment of the new onera 2d icing suite igloo2d. In *9th AIAA Atmospheric and Space Environments Conference*, page 3417, 2017.
[24] Alberto Valli and Alfio Quarteroni. *Domain decomposition methods for partial differential equations*. The Clarendon Press, Oxford University Press, New York, 1999.
[25] James H VanSant. Conduction heat transfer solutions. Technical report, Lawrence Livermore National Lab., CA (USA), 1983.

Appendix A. - Evaporative boundary condition

In sections 4.2 and 5 an evaporative boundary condition is used. It involves two functions $\dot{m}_{ev}(T)$ and $L_v(T)$ representing respectively the rate of evaporation and the latent heat of vaporization which are defined as:

$$L_v(T) = 4185\,(T_{boil} - T) + L_{v,boil} + 1850\,(T - T_{boil}) \tag{A.1}$$

$$\dot{m}_e v(T) = h_m\,(Y_v(T) - Y_v(T_\infty)) \tag{A.2}$$

where

$$h_m = \frac{h_{tc}}{c_{p,air} L_e^{2/3}} \tag{A.3}$$

The Lewis number is defines as the ratio of the Schmidt and Prandtl numbers.

$$L_e = \frac{S_c}{P_r} \tag{A.4}$$

where the Schmidt number is set to $S_c = 0.67$ and the Prandtl number to $P_r = 0.7$.

The vapour mass fraction is linked to the mole fraction and molar masses using:

$$Y_v(T) = \frac{X_v(T)}{X_v(T) + \frac{M_a}{M_v}\,(1 - X_v(T))} \tag{A.5}$$

and the mole fraction is given by:

$$\begin{cases} X_v(T) = \dfrac{p_v(T)}{p_e} & \text{(A.6a)} \\ X_v(T_\infty) = \dfrac{p_v(T_\infty)}{p_\infty} & \text{(A.6b)} \end{cases}$$

Finally, the vapour pressure is given by Sonntag's law:

$$p_v(T) = -\frac{6024.5282}{T} + 29.32707 + 0.010613868\,T - 1.3198825 \times 10^{-5}\,T^2 - 0.49382577\,\log(T) \tag{A.7}$$

Appendix B. - Boundary layer and droplet impingement data for de-icer simulation

The boundary layer and droplet impingement data used for the de-icer simulation were obtained with the IGLOO2D icing code and are shown in Figure B.23. The boundary layer computation is performed with a smooth wall hypothesis.

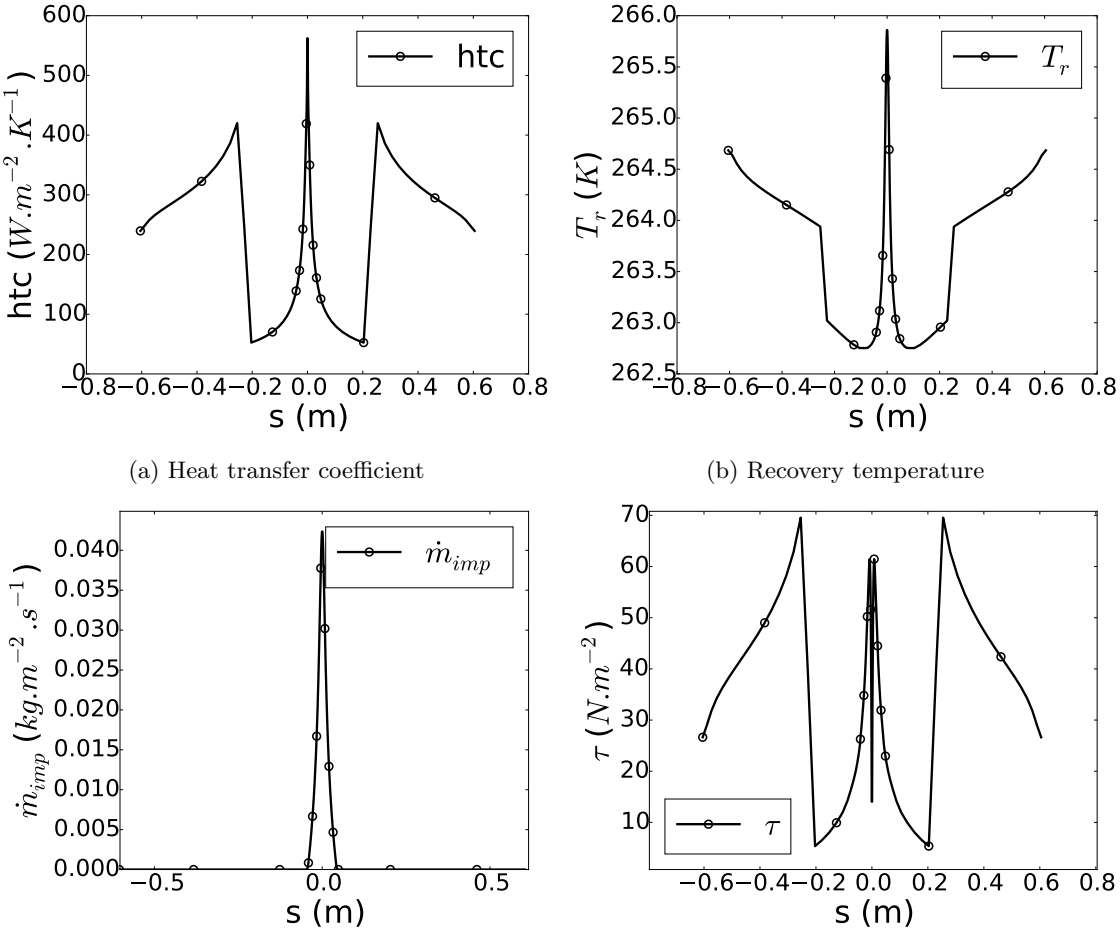

(a) Heat transfer coefficient

(b) Recovery temperature

(c) Droplet impingement rate per unit area

(d) Aerodynamic shear

Figure B.23: Boundary layer and droplet impingement data for de-icer simulation